FRERES MENTOURI UNIVERSITY
CONSTANTINE 1 -ALGERIA

Journal of Sciences & Technology

Semestrial Journal of Freres Mentouri University, Constantine, Algeria

VOLUME 06 - ISSUE 02— DECEMBER 2021

EISSN: ….-….

Freres Mentouri
University Constantine

Ain El-Bey Road
Constantine 25000
Algeria

Phone.Fax: 213 (0) 31. 81. 12.78
Email: revues@umc.edu.dz
Website :http://revue.umc.edu.dz

Journal of Sciences & Technology

Volume 6 N° 2 December 2021

Semestrial Journal of Freres Mentouri University
Constantine, Algeria

SOUMISSION DES ARTICLES

An article proposed for publication should not be submitted at the same time to another journal.

Manuscripts (original and two copies) should be sent to the following address:

Vice-Rectorate in charge of Post-Graduation and Scientific Research

Direction of Publications and Scientific Animation (15th floor)

Constantine 1 University , Aïn-El-Bey Road, 25000 Constantine, ALGERIA.

Tél./Fax: 213 (0) 31.81.12.78

e-mail: revues@umc.edu.dz

Freres Mentouri Constantine1 University

Journal of Sciences & Technology

Volume 6 N° 2 – December 2021

SCIENTIFIC COMMITTEE

INSTRUCTIONS TO AUTHORS

I- Overview

The journal Human Sciences publishes in three languages: Arabic, French and English. Two abstracts must be provided, one in the language of the article, the other in Arabic if the article is written in another language, or in French (or English) if the article is written in Arabic. Abstracts must not exceed 150 words. Unpublished articles are not returned to their authors.

II- Manuscrips

The articles submitted for publication (three copies) must not exceed 20 typewritten pages (tables, figures, graphs, bibliography, ... included) with a large margin to the left (3 cm), printed on 21 x 29 paper , 7 cm (A4) with interligne of good readability. Some flexibility is allowed to authors, but they should organize the text clearly in sections such as: Introduction, Experimental Details, Results, Discussion and Conclusion. The longer articles will be published by part in successive issues, each part being determined by the authors. Authors are kindly requested to accompany the summary of their articles with the most complete possible keywords.

In order to save time and respect deadlines for publication, it is recommended that authors take care of the complete capture of their article on a computer, and send it to the journal, after they have been informed. acceptance for publication, in the form of files on CD.ROM, which will be copied by the service.

However, since the final formatting of the article is done by P.A.O. (Computer Aided Publication), the authors are asked to avoid any formatting of their text. It will be necessary to avoid stylizing it.

III- Bibliography

The bibliographic references quoted in the text must include only the reference number in square brackets (ex .: [5]). If the name of the author appears in the text, it must be followed by the reference number. When the reference contains more than two authors, only the first is cited, followed by "and al".

For articles, the complete reference includes the names of the authors followed by the initials of their first names, the title of the article, the title of the periodical (in conformity with the abbreviations allowed), the volume, the number of the periodical, the year of publication and the relevant pages.

For the works, the reference must include the names of the authors followed by the initials of their first names, the complete title of the work, the volume, the volume, the first and the last page relating to the results discussed, the number of the edition if there are several, the name of the publisher, the place and the year of edition.

For scientific meetings (congresses, proceedings, ...), the reference includes the names of the authors followed by the initials of their first names, the title of the communication, the identification of the meeting, the place, the period and the pages concerned.

IV- Iconography

Tables, boards, charts, maps, photographs, etc. must be provided separately, inset. They must be presented on white sheets of A4 format, individually or in groups, and have underneath the words "table" or "figure" assigned a number.

The illustrations and figures must be clear, professionally made and adequate for reproduction: a 50% reduction, if any, must lead to a suitable size and thickness of characters for good readability. Moreover, for computer-generated figures, in order to maximize contrast, the use of a laser or inkjet printer is essential.

Legends assigned their numbers must be grouped in a separate page.

The final presentation of the article will be left to the discretion of the Editorial Board.

Journal of Sciences & Technology
Volume 6 N° 2– December 2021

SUMMARY

SUMMARY

Journal of Sciences & Technology
Volume 6 N° 2– December 2021

EFFECT OF INCLINATION ANGLE ON THE NATURAL CONVECTION IN A CLOSED ENCLOSURE, DELIMITED BY TWO HORIZONTAL, CENTERED ELLIPTIC CYLINDERS AND TWO DIAMETRICAL PLANS

Submited on 08/01/2013 – Accepted on 09/11/2015

Abstract

The authors present the numerical study of the phenomenon of the natural, laminar and permanent convection in an elliptic annular cavity delimited by two diametrical plans and is tilted at an angle with respect to the horizontal plane. The enclosure considered is of practical interest (Storage, Isolation). It is filled by a Newtonian and incompressible fluid, in laminar and permanent mode. The Prandtl number is fixed at 0.7 (air) but the Grashof number varies. They determine the distributions of the temperature and the stream-function in the fluid and indicate the influence on the flow of the Grashof number and the system tilt.

Keywords: *natural convection / closed enclosure / elliptic cylinders / vorticity-stream function formulation.*

F.BENDJABALLAH
M.DJEZZAR
A.LATRECHE

Energetic Physics Laboratory; Constantine 1 University, Algeria.

Nomenclature

a	Defined constant in the elliptic coordinates, (distance to the poles).	(m)
c_p	Specific heat at constant pressure.	($J.kg^{-1}.K^{-1}$)
e_1	Eccentricity of the internal ellipse.	
Fr	Geometrical factor of form	
$\vec{g}$	Gravitational acceleration.	($m.s^{-2}$)
Gr	Grashof number defined by $Gr = \frac{g\beta a^3}{\upsilon^2}\Delta T$.	
h	Dimensional metric coefficient.	(m)
H	Dimensionless metric coefficient.	
Nu	Local Nusselt number.	
$\overline{Nu}$	Average Nusselt number.	
P	Stress tensor.	
Pr	Prandtl number defined by $\Pr = \frac{\nu \rho c_p}{\lambda}$.	
S_Φ	Source term.	
T	Fluid's temperature.	(K)
T_1	Hot wall temperature.	(K)
T_2	Cold wall temperature.	(K)
ΔT	Temperature deference. $\Delta T=T_1-T_2$.	(K)
V_η, V_θ	Velocity components according to η and θ.	($m.s^{-1}$)
$\vec{V}$	Velocity vector.	($m.s^{-1}$)

Greek letters

α	Inclination angle.	(°)
β	Thermal expansion coefficient.	(K^{-1})
Γ_φ	Diffusion coefficient.	
λ	Thermal conductivity of the fluid.	($W.m^{-1}.K^{-1}$)
υ	kinematic viscosity.	($m^2.s^{-1}$)
ρ	Density.	($kg.m^{-3}$)
η ,θ, z	Elliptic coordinates.	
ψ	function of current.	($m^2.s^{-1}$)
ω	vorticity.	(s^{-1})
φ	General function.	

Superscripts

+	dimensionless parameters.

Subscripts

i	Inner.
e	Outer.
éq	Equivalent
Ni	Points number along the coordinate η
NN	Points number along the coordinate θ
η	According to the coordinate η
θ	According to the coordinate θ

1. Introduction

The study of heat transfer by natural convection, in the annular spaces formed by elliptic cylinders with horizontal axes centered or eccentric, has given rise to many works include such as Zhu et al. (2004) who have made a numerical study into the annulus between two centered elliptic cylinders, using D.Q method (Differential Quadrature) to solve their equations. Djezzar el al. (2004), (2005) and (2006) mean while, have studied numerically natural convection in an annulus formed by two elliptical cylinders and horizontal axes confocal using the formulation in primitive variables, they could detect multi-cellular flows when Grashof number increases, for certain

geometries, and for the three parietal thermal conditions used.

In this work we propose a numerical simulation using the finite-volume method described by Patankar (1980), the elliptic coordinates cited by Moon (1961) and the vorticity stream-function formulation illustrated by Nogotov (1978) to solve the equations governing the phenomenon studied. The mesh adopted for the execution of our calculations is (101x111).

2. Theoretical analysis

We consider an annular space, filled with a Newtonian fluid (in this case air), located between two elliptical cylinders, and two horizontal and centered diametrical planes. Figure 1 represents a cross-section of the system.

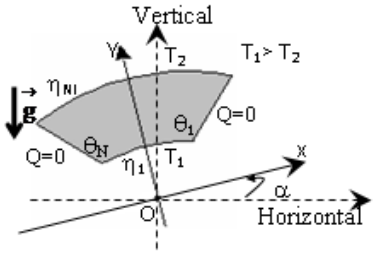

FIG. 1 Cross-section of the system

Both lower and upper walls are elliptical, isothermal and respectively maintained at temperatures T_1 and T_2 with $T_1>T_2$. The two diametrical plans are adiabatic.

It occurs in the enclosure natural convection that we propose to study numerically.

We consider an incompressible fluid flow, two dimensional, permanent and laminar with constant physical properties and we use the approximation of Boussinesq which considers the variations of the density ρ negligible at all terms of the momentum equations except in the term of gravity whose variations with temperature supposed linear, generate the natural convection.

Viscous dissipation and the work of pressure forces are negligible in the heat equation; the radiation is not considered.

With these assumptions the equations governing our problem can be written in vectorial form as follows:

- Continuity equation:

$$\mathrm{div}\,\vec{V} = 0 \qquad (1)$$

- Momentum equation:

$$(\vec{V}.\vec{\mathrm{grad}})\vec{V} = \frac{\rho}{\rho_0}\vec{g} + \frac{\nabla P}{\rho_0} \qquad (2)$$

- Heat equation:

$$(\vec{V}.\vec{\mathrm{grad}})T = \frac{\lambda}{\rho c_p}\nabla^2 T \qquad (3)$$

It is convenient to define a reference frame such as the limits of the system result in constant values of the coordinates. The coordinates known as "elliptic" (η,θ) allow, precisely in our case to obtain this result. Thus the two elliptic isothermal walls will be represented by η_1 and η_{NI} and the two adiabatic walls will be represented by θ_1 and θ_{NN}. The transition from Cartesian coordinates to elliptic coordinates is done using the following relations:

$$\left.\begin{aligned} x &= a.ch(\eta).\cos(\theta) \\ y &= a.sh(\eta).\sin(\theta) \end{aligned}\right\}$$

The equations (1), (2) and (3) are written respectively:

$$\frac{\partial}{\partial\eta}(h V_\eta) + \frac{\partial}{\partial\theta}(h V_\theta) = 0 \qquad (5)$$

$$\frac{V_\eta}{h}\frac{\partial\omega}{\partial\eta} + \frac{V_\theta}{h}\frac{\partial\omega}{\partial\theta} =$$

$$\frac{g\beta}{h}\left\{\begin{aligned} &[F(\eta,\theta)\cos(\alpha) - G(\eta,\theta)\sin(\alpha)]\frac{\partial T}{\partial\eta} \\ &-[F(\eta,\theta)\sin(\alpha) + G(\eta,\theta)\cos(\alpha) +]\frac{\partial T}{\partial\theta} \end{aligned}\right\}$$

$$+\frac{\nu}{h^2}\left(\frac{\partial^2\omega}{\partial\eta^2} + \frac{\partial^2\omega}{\partial\theta^2}\right) \qquad (6)$$

$$V_\eta\frac{\partial T}{\partial\eta} + V_\theta\frac{\partial T}{\partial\theta} = \frac{\lambda}{\rho c_p}\frac{1}{h}\left(\frac{\partial^2 T}{\partial\eta^2} + \frac{\partial^2 T}{\partial\theta^2}\right) \qquad (7)$$

With the introduction of vorticity defined by:

$$\omega = -\frac{1}{h^2}\left(\frac{\partial^2\psi}{\partial\eta^2} + \frac{\partial^2\psi}{\partial\theta^2}\right) \qquad (8)$$

After the introduction of the stream-function, in order to check the continuity equation identically.

$$\left.\begin{aligned} h &= a\left(sh^2(\eta) + \sin^2(\theta)\right)^{1/2} \\ F(\eta,\theta) &= \frac{sh(\eta)\cos(\theta)}{\left(sh^2(\eta) + \sin^2(\theta)\right)^{1/2}} \\ G(\eta,\theta) &= \frac{ch(\eta)\sin(\theta)}{\left(sh^2(\eta) + \sin^2(\theta)\right)^{1/2}} \end{aligned}\right\} \qquad (9)$$

By posing the following adimensional quantities:

D_h= a (arbitrarily selected focal distance)

$$H = \frac{h}{D_h},\quad V_\eta^+ = V_\eta\frac{D_h}{\nu},\quad V_\theta^+ = V_\theta\frac{D_h}{\nu},\quad \omega^+ = \omega\frac{D_h^2}{\nu},$$

$$\psi^+ = \frac{\psi}{\nu} \text{ and } T^+ = \frac{T - T_2}{T_1 - T_2}$$

The equations (5), (6), (7) and (8) becomes:

$$\frac{\partial}{\partial\eta}(H V_\eta^+) + \frac{\partial}{\partial\theta}(H V_\theta^+) = 0 \qquad (10)$$

$$\frac{V_\eta^+}{H}\frac{\partial\omega^+}{\partial\eta} + \frac{V_\theta^+}{H}\frac{\partial\omega^+}{\partial\theta} =$$

$$\frac{Gr}{H}\begin{Bmatrix}[F(\eta,\theta)\cos(\alpha)-G(\eta,\theta)\sin(\alpha)]\dfrac{\partial T^+}{\partial \eta}\\ -[F(\eta,\theta)\sin(\alpha)+G(\eta,\theta)\cos(\alpha)+]\dfrac{\partial T^+}{\partial \theta}\end{Bmatrix}$$
$$+\frac{1}{H^2}\left(\frac{\partial^2\omega^+}{\partial\eta^2}+\frac{\partial^2\omega^+}{\partial\theta^2}\right) \quad (11)$$

$$HV_\eta^+\frac{\partial T^+}{\partial\eta}+HV_\theta^+\frac{\partial T^+}{\partial\theta}=\frac{1}{P_r}\left(\frac{\partial^2 T^+}{\partial\eta^2}+\frac{\partial^2 T^+}{\partial\theta^2}\right) \quad (12)$$

$$\omega^+=-\frac{1}{H^2}\left[\frac{\partial^2\psi^+}{\partial\eta^2}+\frac{\partial^2\psi^+}{\partial\theta^2}\right] \quad (13)$$

The boundary conditions are: For the elliptical hot wall ($\eta = \eta_1$= constant) we have:

$V_\eta^+ = V_\theta^+ = \dfrac{\partial\psi^+}{\partial\theta} = \dfrac{\partial\psi^+}{\partial\eta} = 0$, $T_1^+ = 1$ and

$\omega^+ = -\dfrac{1}{H^2}\left[\dfrac{\partial^2\psi^+}{\partial\eta^2}+\dfrac{\partial^2\psi^+}{\partial\theta^2}\right]$ and for the cold elliptic wall ($\eta=\eta_{NN}$=constant) we have:

$V_\eta^+ = V_\theta^+ = \dfrac{\partial\psi^+}{\partial\theta} = \dfrac{\partial\psi^+}{\partial\eta} = 0$, $T_2^+ = 0$ and

$\omega^+ = -\dfrac{1}{H^2}\left[\dfrac{\partial^2\psi^+}{\partial\eta^2}+\dfrac{\partial^2\psi^+}{\partial\theta^2}\right]$. For the two diametrical plans ($\theta = \theta_1$= constant and $\theta = \theta_{NN}$=constant) we have:

$V_\eta^+ = V_\theta^+ = \dfrac{\partial\psi^+}{\partial\theta} = \dfrac{\partial\psi^+}{\partial\eta} = 0$, $\dfrac{\partial T^+}{\partial\theta}=0$ and

$\omega^+ = -\dfrac{1}{H^2}\left[\dfrac{\partial^2\psi^+}{\partial\eta^2}+\dfrac{\partial^2\psi^+}{\partial\theta^2}\right]$

Once the temperature distribution is obtained; local Nusselt number value is given by the following relation:

$$Nu=-\frac{1}{H}\frac{\partial T^+}{\partial\eta}\bigg|_{\eta=cste} \quad (14)$$

The average Nusselt number is expressed by:

$$\overline{Nu}=\frac{1}{\theta_{NN}-\theta_1}\int_{\theta_1}^{\theta_{NN}}Nu\,d\theta \quad (15)$$

2. 1 Numerical Formulation

To solve the system of equations (11), (12) and boundary conditions, we consider a numerical solution by the finite volumes method. Where as for the equation (13), we consider a numerical solution by the centered differences method.

Both methods are widely used in the numerical solution of transfer problems; they are well exposed by Patankar (1980) and by Nogotov (1978). Figure 2 represents the physical and computational domain.

We cut out annular space according to the directions η and θ from the whole of elementary volumes or "control volume" equal to "$H^2.\Delta\eta.\Delta\theta.1$". (The problem is two-dimensional, the thickness in Z direction is assumed to the unity).

The center of a typical control volume is a point P and center of its side faces "east", "west", "north" and "south", are indicated respectively, by the letters e, w, n and s. Four other control volumes surround each interior control volume. The centers of these volumes are points E, W, N and S. the scalar variables (vorticity, temperature) are stored at centered points in control volumes. Thus transfer equations of scalar variables are integrated in typical control volume.

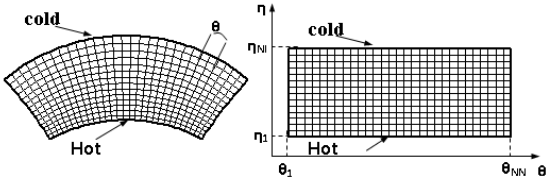

FIG. 2 Physical and computational domain

Figure 3 represents a typical control volume and its neighbors in a computational domain.

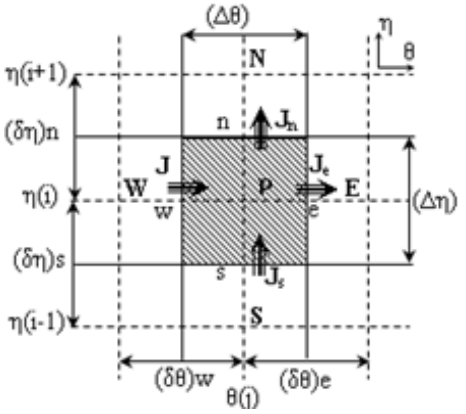

FIG. 3 A typical control volume and its neighbors in a computational domain

2. 2 Discretization of the general transfer equation of a variable φ in the control volume

To illustrate the discretization of the transfer equations by finite volumes method, we consider the transfer equation in its general form:

$$\frac{\partial}{\partial\eta}\left(HV_\eta^+\varphi-\Gamma_\varphi\frac{\partial\varphi}{\partial\eta}\right)+\frac{\partial}{\partial\theta}\left(HV_\theta^+\varphi-\Gamma_\varphi\frac{\partial\varphi}{\partial\theta}\right)=S\varphi \quad (16)$$

Sources and diffusion coefficients are specified in table 1.

Tab. 1 sources and diffusion coefficients of the variables φ

φ	Γ_φ	S_φ
T^+	1/Pr	0
ω^+	1	$\frac{Gr}{h}\left\{\begin{array}{l}\left[F(\eta,\theta)\cos(\alpha)-\mathrm{G}(\eta,\theta)\sin(\alpha)\right]\frac{\partial T^+}{\partial \eta}\\ -\left[F(\eta,\theta)\sin(\alpha)+\mathrm{G}(\eta,\theta)\cos(\alpha)\right]\frac{\partial T^+}{\partial \theta}\end{array}\right\}$

The discretization equation is obtained by integrating the conservation equations over the control volume shown in Figure 3 Patankar (1980), we obtain the following final form:

$$a_P \phi_P = a_N \phi_N + a_S \phi_S + a_E \phi_E + a_W \phi_W + b \qquad (17)$$

The coefficients of equation 17 are well defined by Patankar (1980), the Power Law scheme used to discretize the convectif terms in the governing equations.

3. Results and discussion

We consider two configurations for our cavity characterized by two values of inclination angle (0° and 45°) and a geometrical form factor (Fr = 5) which is defined by:

$$Fr = \frac{\eta_{NI} - \eta_1}{\theta_{NN} - \theta_1}$$

3.1 Grid study

Several grids were used arbitrarily for the following configuration: (α=0° and Fr=1, for $Gr=10^3$, $Gr=10^4$ and $Gr=5.10^4$), to see their effect on the results, table 2 shows us the variation of average Nusselt number and the maximum of the stream function value according to the number of nodes for each grid. We choose the grid (101x111).

Tab. 2 Variation of average Nusselt number and the maximum of the stream-function value according to the number of nodes

	Gr =10³		**Gr =10⁴**		**Gr =5.10⁴**	
$\eta_{NI}x\theta_{NN}$	ψ_{max}	$NU_{moy.}$	ψ_{max}	$NU_{moy.}$	ψ_{max}	$NU_{moy.}$
41x51	0.090	1.387	5.582	2.689	16.575	4.268
51x61	0.090	1.387	5.588	2.685	16.572	4.234
61x71	0.109	1.387	5.593	2.682	16.566	4.197
71x81	0.130	1.387	5.596	2.680	15.560	4.197
81x91	0.179	1.387	5.596	2.678	15.555	4.195
91x101	0.201	1.387	5.596	2.678	15.549	4.190
101x111	0.219	1.389	5.596	2.674	15.549	4.190
111x121	0.219	1.389	5.596	2.674	15.549	4.190

3.2 Numerical code validation

Kuehn et al. (1976) have developed a numerical study on natural convection in the annulus between two concentric and horizontal cylinders with a radius was taken equal to 2.6, they calculated a local equivalent thermal conductivity, defined as being the report of a temperature gradient in a convective and conductive heat exchange on a temperature gradient in an exchange conduction:

$$\lambda_{éq} = \frac{\left.\frac{\partial T^+}{\partial \eta}\right|_{convection+conduction}}{\left.\frac{\partial T^+}{\partial \eta}\right|_{conduction}}$$

They calculated an average value of the conductivity. To validate our numerical code, we compared the average value derived from our calculations with their results. Table 3 illustrates this comparison and we find that quantitatively our results and theirs are in good agreement.

Tab. 3 Comparison of the average thermal conductivity of Kuehn with our results

	Pr	0,70	0,70	0,70	0,70
	Ra	10^2	10^3	$6x10^3$	10^4
Inner wall	Kuehn	1,000	1,081	1,736	2,010
	Presents calculs	1,000	1,066	1,730	2,068
	|E(%)|	**0,000**	**1,388**	**0,346**	**2,886**
Outer wall	Kuehn	1,002	1,084	1,735	2,005
	Presents calculs	1,002	1,066	1,736	2,078
	|E(%)|	**0,000**	**1,661**	**0,058**	**3,641**

3.3 Influence of the Grashof number

3.4 Isotherms and streamlines

Figure 4 and figure 5 represent the isotherms and the streamlines for different values of the Grashof number when α=0°.

We note that these isotherms and these streamlines are symmetrical about the median fictitious vertical plane. These figures show that the structure of the flow is bi-cellular. The flow turns in the trigonometrically direction in the left side and in opposite direction in the right one (the fluid particles move upwards along the hot wall).

For $Gr=10^2$ the isotherms are almost parallel and concentric curves which coincide well with active walls profiles. In this case the temperature distribution is simply decreasing from the hot wall to the cold wall. The streamlines of the fluid show that the flow is organized in two cells that rotate very slowly in opposite directions.

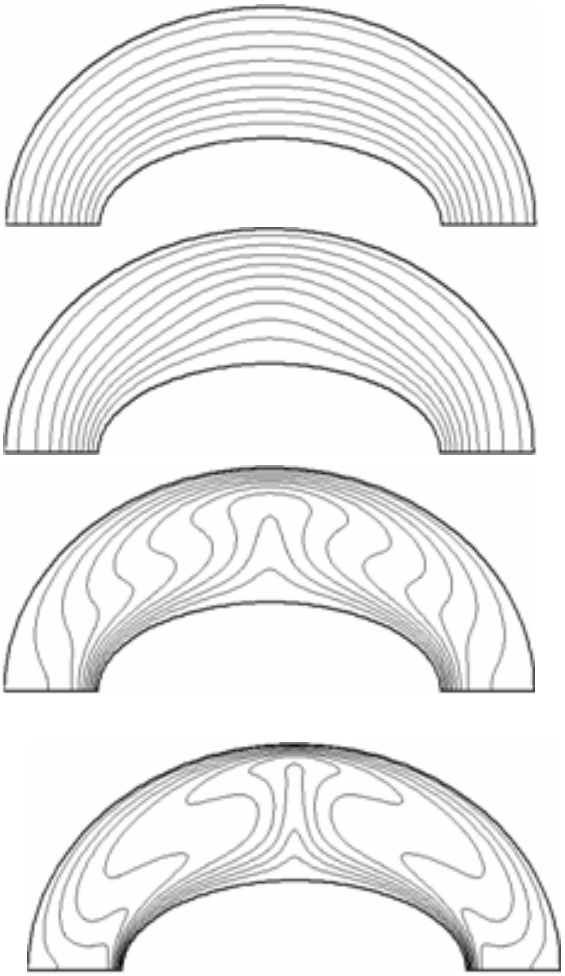

FIG. 4 Isotherms for e_1=0.86, Fr=5, α=0° and respectively Gr=10^2, Gr=10^3, Gr=10^4 and Gr=5.10^4

We can say that the heat transfer is mainly conductive. The values of the streamline which are given on the corresponding figure are very small.

For Gr=10^3 the isothermal lines are transformed symmetrically with respect to the vertical axis and change significantly, and the values of the streamlines mentioned on the same figure, increase also significantly, which translates a transformation of the conductive transfer to the convective transfer, but relatively low as shown in the isotherms shape.

However for Gr=10^4 the isotherms are modified and eventually take the form of a mushroom. The temperature distribution decreases from the hot wall to the cold wall. The direction of the deformation of the isotherms is consistent with the direction of rotation of the streamlines. In laminar flow, we can say that under the action of the particles movement taking off from the hot wall at the symmetry axis, the isotherms move away from the wall there. The values of the stream functions increase which means that the convection intensifies.

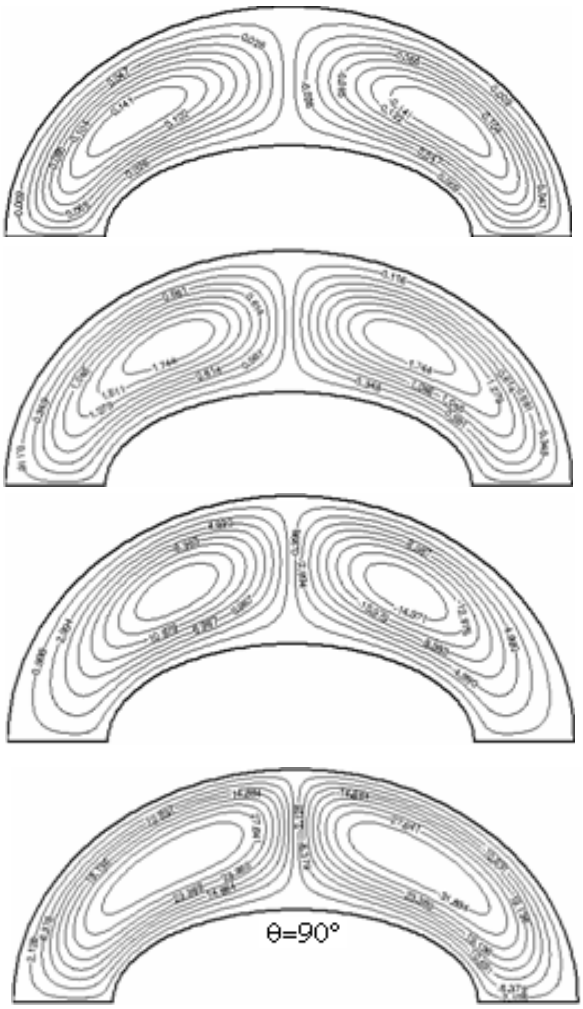

FIG. 5 Streamlines for e_1=0.86, Fr=5, α=0° and respectively Gr=10^2, Gr=10^3, Gr=10^4 and Gr=5.10^4

The increase of the Grashof number to 5.10^4 intensifies the convection as shown in corresponding figures.

Let us note that the isotherms, of all the figures indicated above, were plotted with a ΔT^+=0.1

3.5 Local Nusselt Number

We determine the local Nusselt numbers for which changes along the walls are closely related to the distributions of isotherms and streamlines, so that, qualitatively, these variations and distributions can often be deduced from each other. For example, if we consider a current point on a wall following a coordinated observation of a monotonous reduction in the local Nusselt number corresponds to a directed flow following this coordinate, the observation of an increase corresponds to a directed flow in opposite direction.

3.6 Analogy between the variation of local Nusselt number -isotherms and streamlines

We thus notice on Figure 6, that the variations of local Nusselt number on the inner activate wall are in accordance

with what has just been indicated above, a minimum reflects an existence of two counter-rotating cells pushing away the fluid from the wall, a maximum reflected, on the contrary, the existence of two counter-rotating cells providing the fluid to the wall. What thus enables us to follow the evolution of our flow in our annular space.

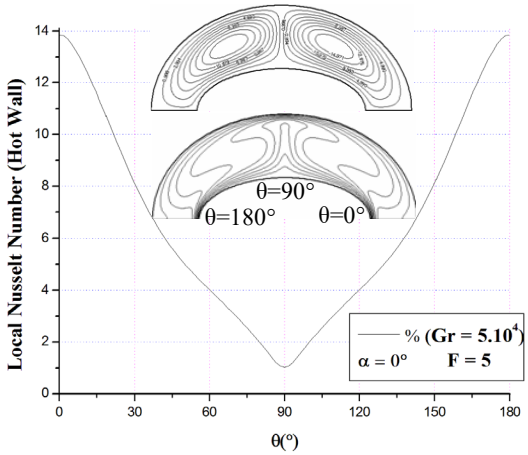

FIG. 6 Variation of local Nusselt number on the inner activate wall

3.7 Variation of local Nusselt number on the hot wall

Figure 7 illustrates the variation of local Nusselt number on the hot wall, and allows us to notice that with the increase of the Grashof number, the value of local Nusselt number on this wall also increases, which is obvious.

3.8 Effect of the angle of inclination α

We examine here the effect of the inclination of the system compared to the horizontal plane, the angle α is measured from the horizontal plane in the trigonometric direction. We used two values of α (0° and 45°).

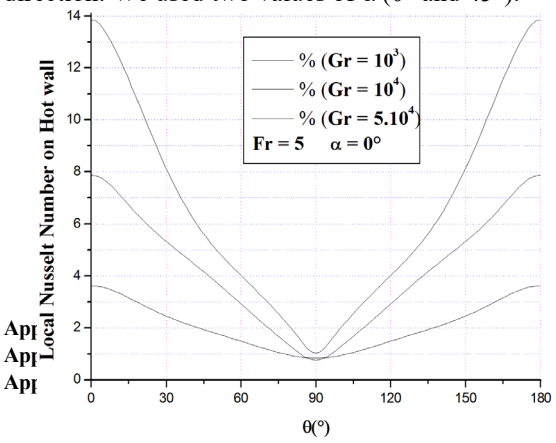

FIG. 7 Variation of local Nusselt number on the hot wall

Appendix D.

3.9 Case where the inclination angle α is zero

In this case, the vertical fictitious median plane is in principle a symmetry plane for transfer phenomena. Therefore by symmetry and in relation to this vertical plane depending on the value of Grashof number, the flow is organized always in two principal cells rotating in opposite directions, as the figures (4-5) show.

3.10 Case where the inclination angle α = 45°

When α=45°, the symmetry of the system relative to the fictitious vertical plane is destroyed as well illustrated in figure 8 and figure 9, the ends of annular space move upwards for the right part of the system and downwards for the left part. Figure 9 show that the cell of left can more develop that its counterpart on the right part and tends to occupy the entire annular space as the system is inclined more until becoming vertical.

3.11 Local and average Nusselt number

The figure 10 which illustrates the variation of local Nusselt number on the hot wall shows that for α=0° the minimum of local Nusselt number is reached at the angular position θ=90°, which is in agreement with figure 5 which shows that the two cells meet at this precise place while moving away the fluid from this wall. For α=45° the minimum of local Nusselt number moves at the position θ=53°, which is in agreement also with figure 9 which shows that for this inclination, the two cells meet at this angular position while moving away the fluid there from this wall.

FIG. 8 Isotherms for e_1=0.86, Fr=5, α=45° and Gr=5.10^4

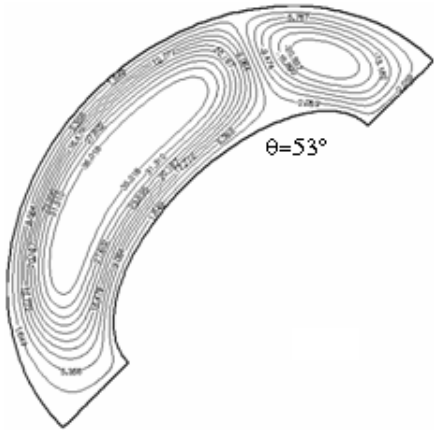

FIG. 9 Streamlines for e_1=0.86, Fr=5, α=45° and Gr=5.10^4

The variation of average Nusselt number on the hot wall as a function of Grashof number illustrated in figure 11 which shows that the inclination α is then without influence when $Gr \leq 10^3$, this translates that the heat transfer is primarily conductive. For the greatest values of the Grashof number, α influences the convective transfer.

CONCLUSION

We established a mathematical model representing the transfer of movement within the fluid and heat through the active walls of the enclosure. This model based on the assumption of Boussinesq and the bidimensionnality of the flow. We have developed a calculation code, based on the finite volume method, which determines the thermal and dynamic fields in the fluid and the dimensionless numbers of local and average Nusselt on the active walls of the enclosure, depending to the quantities characterizing the state of the system. The influence of the Grashof number and the inclination of the system, on the flow in stationary mode has been particularly examined.

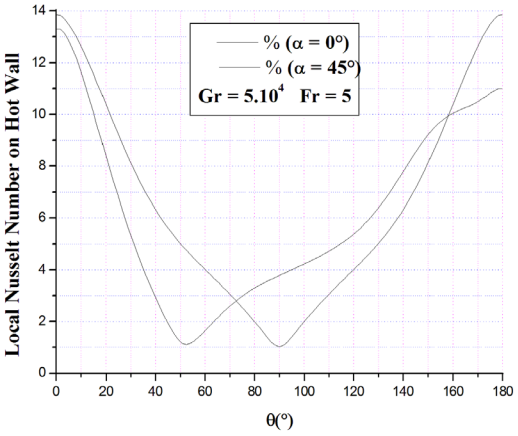

FIG. 10 Variation of local Nusselt number on the hot wall

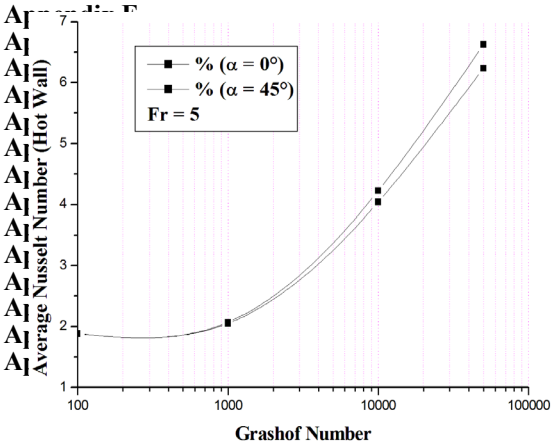

FIG. 11 Variation of the average Nusselt number on the inner activate wall

Appendix S.

The results of the numerical simulations have shown that conduction is the regime of heat transfer dominant for Grashof numbers lower than 10^3. For Grashof numbers higher than 10^3, the role of the convection becomes dominant, this on the one hand, on the other hand we saw that the transfers are better when our system presents elements of symmetry.

Appendix T.

REFERENCES

[1] T.H.Kuehn, R.J. Goldstein, An experimental and theoretical study of natural convection in the annulus between horizontal cylinders, J. Fluid Mech., 74, 695-719, 1976.

[2] Y.D.Zhu, C. Shu, J. Qiu, J. Tani,Numerical Simulation of natural convection between two elliptical cylinders using DQ method, Int. J. Heat. Mass. Trans., 47, 797-808, 2004.

[3] M.Djezzar,M. Daguenet, Numerical study of bidimensional steady natural convection in a space annulus between two elliptic confocal ducts. 1ST International Conference on Thermal Engineering Theory and Applications. Beïrut-Lebanon, du 31 Mai au 04 Juin, 2004.

[4] M.Djezzar,M. Daguenet, Contribution to the study of the convection in various annular spaces, subjected to various conditions of heating. Thesis of Doctorate of state, University Mentouri Constantine, 2005.

[5] M.Djezzar,A. Chaker,M. Daguenet, Numerical study of bidimensional steady natural convection in a space annulus between two elliptic confocal ducts: Influence of internal

Appendix U. eccentricity. Revue des Energies Renouvelables. 8, 63-72, 2005.

[6] M.Djezzar,M. Daguenet, Natural steady convection in a space annulus between two elliptic confocal ducts: Influence of the slope angle. Journal of Applied Mechanics Transaction of the ASME, 72, 88-95, 2006.

[7] S.V.patankar , Numerical Heat Transfer and fluid flow, (McGraw-Hill book company), ppc113-137. New York,1980.

[8] P.Moon, E. Spencer, Field theory Engineers, (D. VAN. Nostrand company), p 356. LTD, Torronto,, Canada , 1961.

[9] E.F.Nogotov, Applications of Numerical Heat Transfer, (McGraw-Hill book company), ppc122-125. New York, 1978.

I-

BETA DECAY HALF-LIVES AND RATES OF $^{134-136}$SN NUCLEI

M. KHITER and F. BENRACHI

Laboratoire de Physique Mathématique et Subatomique, Département de Physique, Faculté des Sciences Exactes, Université des frères Mentouri Constantine-1 (Algérie).

Reçu le 07/06/2014 – Accepté le 11/11/2015

Abstract

In astrophysical environment, allowed Gamow-Teller (GT) transitions and space phase factors play an important role in determination of transition rates and half-lives, particularly for β-decay in presupernova evolution of massive stars. The estimation of these half-lives in neutron rich nuclei is needed in astrophysics for the understanding of supernovae explosions and the processes of nucleosynthesis, principally the r-process, and in the experimental exploration of the nuclear landscape. Their determination in agreement with experimental results is a challenging problem for nuclear theorists. In this work, the total β-decay half-lives and rates of 134-136Sn nuclei at different temperatures are calculated using various interactions developed in the light of recently available information on experimental binding energies and low-lying spectra of Sn, Sb and Te isotopes in 132Sn mass region. The calculation has been realized using Oxbash code in the frame work of the nuclear shell model. With these interactions, one can observe that the effective half-lives increase and the total decay rates decrease with increasing temperature. A deviation of half-lives starts at around 0.2 MeV and satures above 10 MeV, but the half-lives limit values are slightly different for all interactions.

Keywords: β decay half-lives and rates, Gamow-Teller, Oxbash code, 132Sn region.

Résumé

Dans l'environnement astrophysique, les transitions permises de Gamow-Teller (GT) et les facteurs d'espace de phase jouent un rôle important dans la détermination des taux de transition et des demi-vies, en particulier pour la désintégration β dans l'évolution des étoiles massives des supernova. L'estimation de ces demi-vies dans les noyaux riches en neutrons est nécessaire en astrophysique pour la compréhension des explosions de supernovae et des processus de nucléosynthèse principalement dans le processus r, et dans l'exploration expérimentale de la charte nucléaire. Leur détermination en accord avec les résultats expérimentaux est un problème difficile pour les théoriciens nucléaires. Dans ce travail, les demi-vies totales et les taux de transition des noyaux 134-136Sn sont calculés en fonction de la température à l'aide de différentes interactions développées sur la base d'information récente sur les énergies de liaison expérimentales et les spectres des isotopes Sn, Sb et Te dans la région de masse 132Sn. Les calculs ont été réalisés au moyen du code Oxbash dans le cadre du modèle en couches nucléaires. Avec ces interactions, on observe que les demi-vies effectives augmentent et les taux de décroissance diminuent avec l'accroissement de la température. La déviation des demi-vies commence à environ 0,2 MeV et sature au dessus de 10 MeV, mais les valeurs limites des demi-vies sont légèrement différentes.

Mots clés *: Désintégration β-, demi-vies et taux de transition, Gamow-Teller, code Oxbash, région de 132Sn*.

ملخص.

في البيئة الفلكية، الانتقالات المسموحة *(GT Gamow-Teller)* وعوامل طور الفضاء تلعب دورا هاما في تحديد معدلات الانتقال وأنصاف العمر، ولا سيما في التفكك *β* لتطور النجوم الضخمة في *supernova* . تقدير ا نصاف العمر في الانوية الغنية بالنيوترونات ضروري في الفيزياء الفلكية لفهم انفجارات *supernova* وعمليات الاصطناع النووي بشكل رئيسي في الظاهرة *r*، وفي الاستكشاف التجريبي على الخريطة النووية. تقديراتهم على اتفاق مع النتائج التجريبية مشكلة صعبة بالنسبة للنظرين النوويين. في هذا العمل يتم حساب انصاف العمر الكلية ومعدلات الانتقال في الانوية *Sn*136-134 بدلالة درجة الحرارة باستخدام تفاعلات مختلفة وضعت على اساس معلومات حديثة تقوم على طاقات الربط التجريبية والأطياف للنظائر *Te*و*Sb, Sn* في المنطقة *Sn*132. تم إجراء الحسابات في اطار النموذج الطبقى بواسطة برنامج البنية النووية *Oxbash* مع هذه التفاعلات، لوحظ أن انصاف العمر الفعالة تزداد ومعدلات التفكك تنخفض مع زيادة درجة الحرارة. يبدأ الانحراف لأنصاف العمر بحوالي *MeV0.2* ويدرك التشبع ابتداء من *MeV*10، ولكن قيم التشبع لأنصاف العمر مختلفة ببطء.

الكلمات المفتاحية: **التفكك *β* -انصاف العمر ومعدلات التفكك ، *Gamow-Teller* ،البرنامج *Oxbash*، المنطقة *Sn*132.**

Introduction:

The neutron-rich nuclei with few valence nucleons above the doubly closed ^{132}Sn core are interesting to extract empirical NN interaction and test the theoretical description of the nuclear structure shell model in this mass region [1]. The study of structure properties of these nuclei aims to gathering new data on decay of *Sn* isotopes beyond the magic ^{132}Sn nucleus. These are of a great interest for modeling r-process [2], and comprehension the element abundances in the universe [3]. For *r-process* nucleosynthesis, β^- decay of neutron rich nuclei becomes important when the timescale of neutron capture is comparable to that of the photodisintegration in the vicinity of the neutron shell gaps N= 50, 82 and 126 [4]. Beside, these neutron closed shells, the *r-process* comes closest to the line of β stability and falls on the waiting point isotopes, where the β-decay half-lives are the longest in the r-process path [5].

In the waiting point approximation, an (n,γ) and (γ,n) thermal equilibrium is assumed to be established in the nuclei inside an isotopic chain. Only β-decay half-lives and neutron binding energies are needed [5,6]

Calculations

Large basis calculations are carried out by means of *Oxbash* nuclear structure code [7], in the framework of the shell model. In these calculations, the Z50N82 valence space consisting of $\pi(1g_{7/2}, 2d_{5/2}, 2d_{3/2}, 3s_{1/2}, 1h_{11/2})$ and $\nu(1h_{9/2}, 2f_{7/2}, 2f_{5/2}, 3p_{3/2}, 3p_{1/2}, 1i_{13/2})$ orbitals above the ^{132}Sn core is used with *kh5082* [8], *cw5082* [8], *cwg* [9] , *smpn* [10], *kh3, cwΔ5082* [11] and *khΔ5082* [12] (1+2)-body Hamiltonians.

In the two latest ones, we carry out some modifications based on the *N-N* pairing interaction [13]. The *p-n* tbme, corresponding to eight excited states 0^-, 1^-, 2^-, 3^-, 4^-, 5^-, 6^-, and 7^- of the original *kh5082* interaction [8], have been modified using the renormalization factor 0.74. For *n-n tbme*, we modified those corresponding to 0^+ and 2^+, 4^+, 6^+, 8^+ excited states, using 0.48 and 0.6 renormalization factors respectively [14]. While, the *p-p* tbme modification correspond to 0^+, 2^+, 4^+ and 6^+ excited states, with 1.08 renormalization factor [10].These renormalization factors, reflecting the reduction of pairing in first excited states, were adjusted to experimental data in the *Sn*, *Sb* and *Te* isobars. The proton and neutron *SPE* are taken from Ref [15]. In the present work, an estimation of the depressed energies effect on β^- decay rates of the exotic even *Sn* isotope ($^{134\text{-}136}Sn$) above the ^{132}Sn core have been calculated. In order to obtain the necessary *ft* values corresponding to the decay of thermally populated excited states of the mother to the excited states of the daughter nucleus, the calculation of reduced transition probabilities are needed. In the case of neutron rich nuclei, only Gamow-Teller transitions can occur. Indeed, the allowed Fermi transitions in the isobaric analogue states ($\Delta T=0$) are located at an excitation energy higher than that of the ground state of the mother nucleus, outside the energetic window Q_β. So, it is impossible to observe Fermi transitions in the side of neutron rich nuclei. The excitation energies and the transition densities of $^{134\text{-}136}Sn$ and $^{134\text{-}136}Sb$ nuclei are calculated using cited interactions, in order to evaluate $B(GT)$ values required in the calculation of beta decay rates. It is known that the thermal population of excited nuclear levels becomes more important with increasing temperature and lower excitation energy. In the situation of pre-supernovae, the temperature of nuclei is so high that the beta decay rate of a nucleus in this astrophysical environment depends on it. Also, one can express it by this formula [16,17]:

$$\lambda = \frac{\ln 2}{\kappa}\sum_i \frac{(2J_i+1)e^{\left(\frac{-E_i}{kT}\right)}}{G_i(z,A,T)}\sum_j B_{ij}\phi_{ij} \qquad (1)$$

where the sums in i and j run over states in the mother and daughter nuclei respectively. The constant κ=6250 s [18 ,19], and G_i denote the partition function of the mother nucleus defined as,

$$G_i(z,A,T) = \sum_i (2J_i+1)e^{-E_i/kT} \qquad (2)$$

Here, B_{ij} are the reduced transition probabilities given as a function of Gamow-Teller and Fermi transition probabilities by

$$B_{ij} = B_{ij}(GT) + B_{ij}(F) \qquad (3)$$

Gamow Teller B_{ij}(GT) and Fermi B_{ij}(F) transition probabilities are defined as [17, 19]:

$$B_{ij}(GT) = \left(\frac{g_A}{g_V}\right)^2_{bare} \frac{\left|\left\langle J_f \left\| \sum_i \sigma(i) t_-(i) \right\| J_i \right\rangle\right|^2}{2J_i+1}$$

$$B_{ij}(F) = \frac{1}{2J_i+1}\left|\left\langle J_f \left\| \sum_i t_-(i) \right\| J_i \right\rangle\right|^2 \qquad (4)$$

here $t_-(i)$ and $\sigma(i)$ stand for the isospin and spin vectors of the i^{th} nucleon. J_f and J_i denote respectively the final and initial angular momenta, and g_A, g_V are vector and axial-vector coupling constants such as [19]:

$$\left(\frac{g_A}{g_V}\right)_{bare} = 1.25 \qquad (5)$$

The last factor in Eq. (1), ϕ_{ij}, is the phase space integral for which the approximation method is described in [17,20].

In a transition β^-, the values of the reduced transition probabilities from the state of the mother to the state of the daughter are used to determine the value of *ft* which is given as[19]:

$$ft = \frac{\kappa}{B_{ij}(GT) + B_{ij}(F)} \qquad (6)$$

Results and Discussion

III-1 Spectra

Several data are accumulated in the tin 132 region, exceptionally the single particle energies (SPE). The ^{134}Sb nucleus have one proton and one neutron in addition to the tin core. Its low lying proton-neutron states have the configuration ($\pi 1g_{7/2}\nu 2f_{7/2}$). The 0^-, 1^-, 2^- and 3^- excited states are observed in the β^- decay of the ^{134}Sn *[21]*, while the state 7^- is populated by means of $\beta^- n$ decay in ^{135}Sn [22]. The spectrum of isotope ^{134}Sn have been observed in prompt γ-radiation fission fragments from ^{248}Cm. The first three excited states were interpreted as members of the $\nu(2f_{7/2}\ ^2)$ multiplet [23].

The isotope ^{136}Sb had been first observed as a β-*n* delayed precursor produced in thermal neutron induced fission of ^{235}U, and it has been produced in the projectile fission of ^{138}U at the relativistic energy of 750 *MeV/u* on ^{9}Be target [24].

Very recently, experiments were carried out at the RIKEN Radioactive Isotope Beam Factory (RIBF) [25, 26] to study the neutron rich isotopes of Sn. In one of the experiments the first 2^+ excited state in the neutron-rich tin isotope ^{136}Sn has been identified at 682(13) keV by measuring γ-rays in coincidence with the one proton removal channel from ^{137}Sb [25]. The calculated energetic spectra (low energies) in comparison with the experimental one of the parent and daughter nuclides are illustrated in Fig.1 and 2.

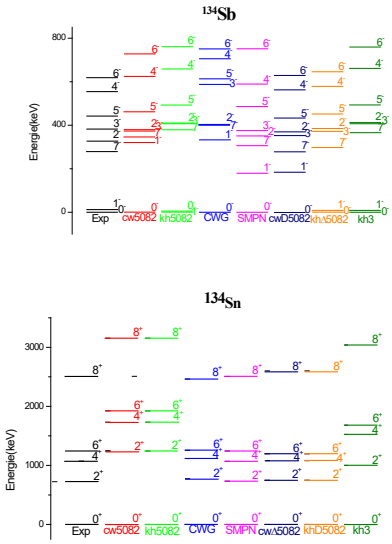

Fig 1: Calculated energetic spectrum using *kh5082*, *cw5082*, *cwg*, *smpn*, *kh3*, *cwΔ5082* and *khΔ5082* in comparison with experimental for ^{134}Sn and ^{134}Sb nuclei.

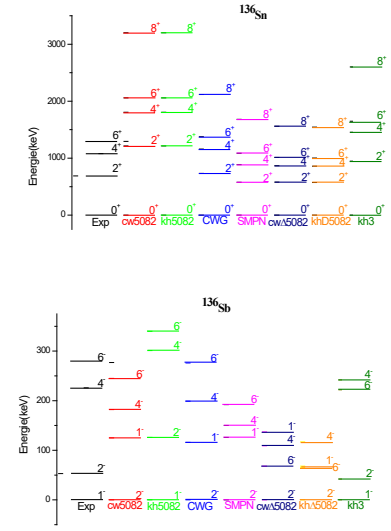

Fig 2: Calculated energetic spectrum using kh5082, cw5082, cwg, smpn, kh3, cwΔ5082 and khΔ5082 in comparison with experimental for 136Sn and 136Sb nuclei

These figures show that the getting results using the various interactions are in good agreement with the experimental data for ^{134}Sn and ^{134}Sb nuclei: the khΔ5082 interaction. However, for 136Sn and ^{136}Sb nuclei, CWG and kh3 interactions reproduced well the experimental spectrum respectively.

III-2 Half lives

The relevant information, for these isotopes incorporated for modifications in the decay rates that result from inclusion of excited states due to thermal excitations, are shown in Table 1. The figures 3 and 4 show relative energies of $^{134\text{-}136}$Sn and $^{134\text{-}136}$Sb nuclei respectively and β^- decays between different levels.

Table 1: Relevant information used the calculations.

Mother	Exp$_{\text{Half-life}}$ (s)	Q_{Value} MeV	Mother (*Sn*) tates	Daughter (*Sb*) States
^{134}Sn	1.05	7.37	2_1^+, 2_2^+	3_1^+, 1_1^+, 2_1^+, 2_2^+, 3_2^+
^{136}Sn	0.25	8.37	2_1^+, 2_2^+	3_1^+, 1_1^+, 2_1^+, 2_2^+, 3_2^+

The selection rules for GT transitions only allow transitions from single particle $\nu 1h_{9/2}$ orbital to $\pi 1h_{11/2}$ orbital in this model space. But the wave function compositions of the relevant low lying states in these isotopes of *Sn* and *Sb* have very small contribution from the shell model configurations involving these orbitals. So the calculated allowed GT strengths are generally very small.

We have also calculated the Gamow-Teller strengths and the half-lives in the temperature range from T= 0.01 to 100 *MeV* (fig.3 and 4).

While varying the temperature in the nuclear field going from 10 *keV* to 100 *MeV*, one can observe that for the interactions, the effective half-life increases with increasing temperature for $^{134\text{-}136}Sn$.

However, the total rate decreases with increasing temperature. The rate partial of decay starting from the fundamental state (0^+) is quite fast and those starting from the excited states 2_1^+ and 2_2^+ are of two orders of magnitude slower for (kT=1*MeV*), as the beta decay from ground state to ground state of daughter is forbidden, but it is quite fast. In the range 0.01 *MeV* to 0.2 *MeV*, $T_{1/2}$ is constant at ~ 1.05 s (^{134}Sn) or ~ 0.25 s (^{136}Sn) corresponding with that obtained in laboratory measurements. Beyond 0.2 *MeV* (~10^9K), there is a deviation of this value for all interactions used. The deviation starts at the same temperature and the saturation is reached above 10 *MeV*. The limit values in ^{134}Sn isotope varied between 3s and 9s while in ^{136}Sn isotope they have a value around 2.5 s.

CONCLUSION

In this paper, we calculate the excitation energies, beta decay half-lives and transition rates for A=134-136 isobars with two and four valence particles in addition to the ^{132}Sn ($^{134\text{-}136}Sn$ and $^{134\text{-}136}Sb$ nuclei). The calculations are carried out in the framework of the shell model by means of *Oxbash* nuclear structure code, using *kh5082*, *cw5082*, *cwg*, *smpn*, *kh3*, *cwΔ5082* and *khΔ5082* interactions. The new experimental values of the single particle energies were used. The getting results using the various interactions are in good agreement with the experimental data in the case of ^{134}Sn *and* ^{134}Sb nuclei : the khΔ5082 interaction. While for the case of ^{136}Sn *and* ^{136}Sb nuclei, CWG and kh3 interactions reproduced well the experimental spectrum respectively. With these interactions, the deviation and saturation of half-lives start respectively at around 0.2 *MeV* and above 10 *MeV*. The limit values in ^{134}Sn *and* ^{136}Sn isotopes are 3s and 2.5 s respectively.

Acknowledgement

Special thanks are owed to B. A. Brown for his help in providing us the OXBASH code (Windows Version) …
Authors thanks Pr. M. Saha Sarkar.

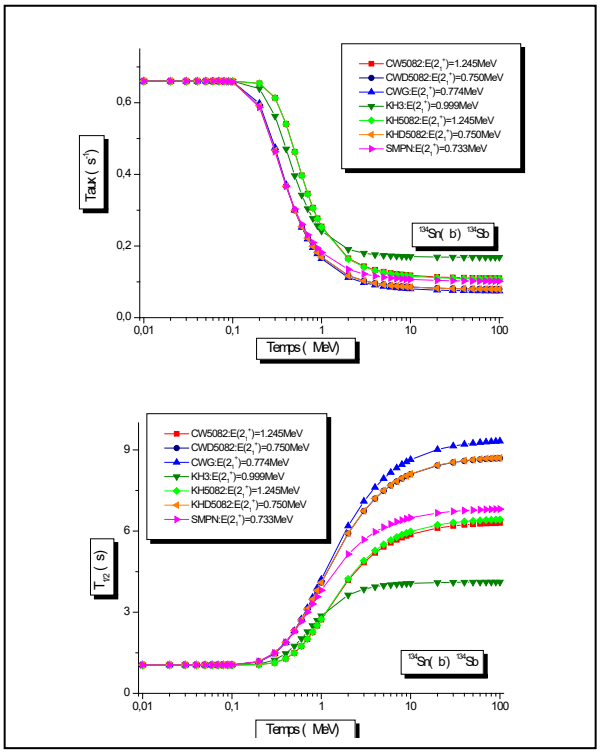

Fig 3: β decay rates and half-lives as a function of temperature for ^{134}Sn

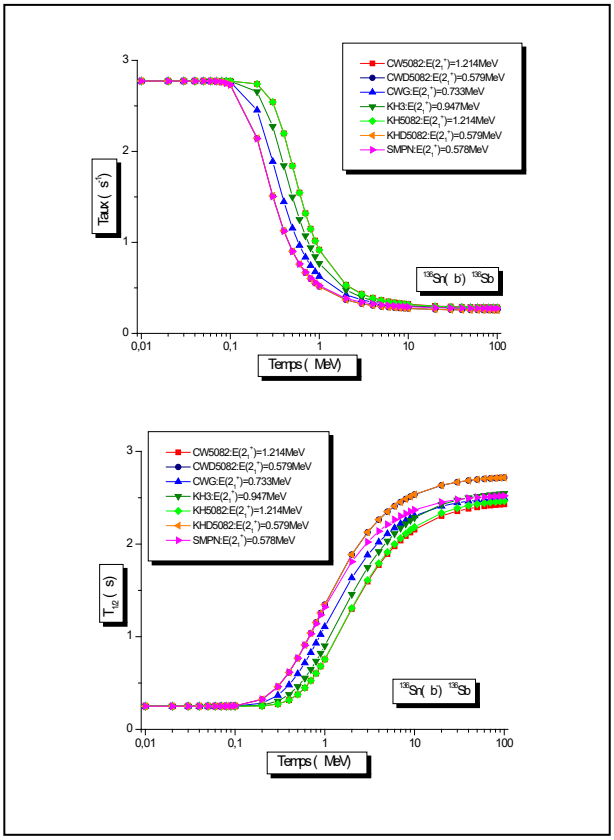

Fig 4: β decay rates and half-lives as a function of temperature for ^{136}Sn

REFERENCES

[1]. J. Blomoqvist, "Single-Particle States Around Double-Magic ^{132}Sn" Proceedings of the 4th International Conference on Nuclei Far from Stability, *CERN, Geneva report N° 81-09, (1981)pp. 536.*

[2]. L. Coraggio et al .,"Erratum : Shell-model structure of exotic ^{135}Sb", *Phys. Rev. C**72**, 057302 (2005).*

[3]. H. Grawe et al., "Shell structure from 100 Sn to 78 Ni: Implications for nuclear astrophysics", *Eur. Phys. J. A**25**, 357 (2005).*

[4]. F. Minato and K. Hagino"β-decay half-lives at finite temperatures for N=82 isotones", *Phys. Rev. C**80**, 065808 (2009).*

[5]. K. L. Kratz et al., "Gamow-Teller decay of ^{80}Zn : shell structure and astrophysical implications", *Phys. Rev. C**38** ,1 (1988).*

[6]. G. Baur et al.,"Electromagnetic dissociation as a tool for nuclear structure and astrophysics", *Prog. in Part. and Nucl. Phys.**51**, 487 (2003).*

[7]. B. A. Brown, A. A. Etchegoyen and W. D. H. Rae , NS. Godwin, "code OXBASH (unpublished)", *MSU-NSCL Report No. 524, (1985).*

[8]. W. T. Chou and E. K. Warburton,"Construction of shell-model interactions for Z≥ 50, N ≥82 nuclei: Predictions for A=133-134 β^- decays" , *Phys. Rev. C45, 1720 (1992).*

[9]. B. A. Brown et al., "Magnetic moments of the 2^+_1 states around ^{132}Sn" *Phys. Rev. C 71, 044317 (2005).*

[10]. S. Sarkar, M. Saha Sarkar "Shell Model Calculations with Modified Empirical Hamiltonian in ^{132}Sn region", *Eur. Phys. J. A 21, 61 (2004).*

[11]. L. Aissaoui et al.," Pairing gap energy correction in Shell model for the neutron-rich tin isotopes", *Braz. J. of Phys., vol. 39, n° 4 (2009).*

[12]. N. Laouet et al., "Proton-Neutron Pairing Interaction in Neutron Rich A = 132 Nuclei", AIP *Conf. Proc. 1295, 230 (2010).*

[13]. G. Audi et al., "The AME2003 Atomic Mass Evaluation : Tables, Graphs and References", *Nucl. Phys. A 729, 337 (2003).*

[14]. J. Terasaki et al.," Anomalous behavior of 2^+ excitations around^{132}Sn", *Phys. Rev. C 66, 054313 (2002).*

[15]. B. Fogelberg et al., "Precise Atomic Mass Values near ^{132}Sn: the resolution of a puzzle", *Phys. Rev. Lett. 82, 1823 (1999).*

[16]. M. Chernykh et al., "The Role Of The 96 keV Level In The^{19}O(β^-)^{19}F Process At Stellar Temperatures", *The Astrophys. Jour. 633, L61 (2005).*

[17]. K. Langanke and G.M. Pinedo, "Rate tables for the weak processes of pf-shell nuclei in stellar environments", Atom. Data and Nucl. Data Tables 79 (2001).

[18]. A. Aprahamian et al., "Nuclear structure aspects in nuclear astrophysics", Prog. in Part. and Nucl. Phys. 54, 535 (2005).

[19]. K. Kar et al.,"Beta-Decay Rates of fp Shell Nuclei with A> 60 in Massive Stars at the presupernova stage", *The Astrophys. Jour. 434, 662 (1994).*

[20]. N. B. Gove and M.J. Martin,"Log-f Tables for beta decay", *Nucl. Data Tables 10 (1971).*

[21]. A. Korgul et al., "The neutron and proton two-particles nucleus ^{134}Sb: New low-spin states observed in the decay of ^{134}Sn and an estimate of the energy of the 7^- isomer ", Eur. Phys. J. A 15, 181 *(2002).*

[22]. J. Shergur et al.,"Level structure of odd-odd ^{134}Sb populated in the beta decays of ^{134,135}Sn", *Phys. Rev. C 71, 064321 (2005).*

[23]. A. Korgul et al., "Properties of N=84, even-even nuclei populeted in *the spontaneous fission of 248Cm", Eur. Phys. J. A 7, 167 (2000).*

[24]. *M.N.* Mineva et al., "A new μs isomer in ^{136}Sb produced in the projectile fission of ^{238}U", *Eur. Phys. J. A 11, 9 (2001).*

[25]. He Wang et al., " Structure of ^{136}Sn and the Z = 50 magicity", *Prog. Theor. Exp. Phys. 023D02 (2014).*

[26]. G. S. Simpson et al.," Yrast 6^+ Seniority Isomers of ^{136,138}Sn", *Phys. Rev. Lett. 113, 132502 (2014).*

TRANSIENT LAMINAR SEPARATED FLOW AROUND AN IMPULSIVELY STARTED SPHERICAL PARTICLE AT 20≤RE≤1000

BENABBAS FARIDA AND BRAHIMI MALEK

University A. MIRA of Bejaïa, Faculty of Technology, Department of Process Engineering, Targa-Ouzemour,Bejaia,Algeria

Reçu le 02/08/2013 – Accepté le 24/06/2015

Abstract

Numerical simulations of the axisymmetric laminar flow characteristics past a rigid sphere impulsively started are presented for Reynolds numbers from 20 to 1000. The results are obtained by solving the complete time dependant Navier-Stokes equations in vorticity and stream function formulation. A fourth order compact method is used to discretize the Poisson equation of stream function while the vorticity transport equation is solved by an alternating direction implicit method. Time evolution of flow separation angle and length of the vortex behind the sphere are reported. Time variation of the axial velocity in the vortex and the wall vorticity around the sphere are also examined. Secondary vortices are seen to be initiated at Reynolds number of 610 and for dimensionless time t about 5. Comparisons with previously published simulations and experimental data for steady state conditions show very good agreement.

Mots clés : transient flow, hermitian compact, vortex length, drag, sphere

Résumé

Les simulations numériques des caractéristiques de l'écoulement laminaire axisymétrique autour d'une sphère rigide en démarrage impulsif, sont présentées pour des nombres de Reynolds variant entre 20 et 1000. Les résultats sont obtenus par résolution de l'équation de Navier-Stokes complète, instationnaire dans sa formulation rotationnel-fonction de courant. Un schéma numérique compact précis à l'ordre 4 est utilisé pour la discrétisation de l'équation de Poisson pour la fonction de courant et est combiné à la méthode implicite aux directions alternées pour l'équation de transport de la vorticité. Nous présentons l'évolution temporelle de l'angle de séparation et de la longueur du tourbillon. Nous examinons aussi la variation au cours du temps de la vitesse axiale et de la vorticité autour de la sphère. Le tourbillon secondaire est initié au temps adimensionné 5 pour un Reynolds proche de 610. Les données numériques et expérimentales, dans le cas stationnaire, disponibles dans la littérature présentent une bonne concordance avec nos résultats.

Keywords: Ecoulement transitoire, hermitian compact, longueur de vortex, sphere.

ملخص.

محاكاة عددية لخصائص الانسياب الطبقي المتماثل محوريا حول جسم كروي صلب دو الحركة الدافعة مقدمة لأعداد رينولدس بين 20 و 1000 .تحصلنا على النتائج بتحليل معادلة نافيي ستوكس الكاملة و المحظرة على شكل دالة التيار والدوران الدوامي.

طريقة التفصيل العددي المستعملة لتحليل معادلة بواسون بدقة من الدرجة الرابعة هي طريقة متضامه استعملت بسياق طريقة "الاديئي" .

نقدم نتائج التطور الزمني لزاوية الانفصال السيلان من الجسم الكروي و طول الحركة الدوامية. قدمنا كذالك التطور مع الزمن للسرعة المحورية داخل الدوامة و قيمة الدوامة على سطح الجسم الكروي. بينت المحاكاة العددية ميلاد الدوامة الثانوية قرابة عدد رينولدس 610 في الزمن 5 .

المقارنات مع المحاكاة المنشورة سابقا والبيانات التجريبية تبين أتفاقا جيد بالنسبة للسيلان المستقر.

الكلمات المفتاحية: تدفق عابرة، الهرميتي المدمجة، طول دوامة، المجال

Introduction :

The steady and unsteady viscous flows over a spherical particle have been extensively studied by different numerical approaches and experimental methods (Rimon and Cheng (1969),Benabbas (1987) Fornberg (1988), Johnson and Patel (1999), Lee (2000), Benabbas et al. (2003), Gushchin and Matyushin (2006), Sekhar et al. (2012)). The transient development of the momentum transfer or heat and mass transfer around a sphere has received rather much less attention (Benabbas and Brahimi (2012)). The accelerating conditions of the particle motion have been considered in numerical studies at moderate Reynolds numbers (Lin and Lee (1973), Reddy et al. (2010)). In the present paper, the time evolution of the flow induced by an impulsively started sphere is considered for Reynolds numbers up to 1000. This case constitutes a reference model for more complex practical situations such as the behaviour of the flow around particles in fluidizing systems (Kechroud et al. (2010a,b)). Similar problem for the cylinder has been investigated numerically (Ta Phuoc Loc and Bouard (1985), Thoman and Szewczyk (1969), Collins and Dennis (1973) and experimentally (Bouard and Coutanceau (1980)). A very good agreement between the simulations and the experimental results was observed including the complex structure of the secondary vortices. We have used the same efficient numerical method to conduct the analysis of the separated laminar flow over a sphere. The numerical method is based on a high-order compact scheme for spatial discretization of the stream function equation and a second-order one (ADI) to handle the vorticity equation while the time discretization is of second-order accuracy. The transient development of the flow is examined through the presentation of its main characteristics. Time evolution of the separation angle with Reynolds number is presented. The wall vorticity behavior for increasing time and Reynolds number is analyzed. The length of the recirculation region with time behind the sphere is also reported. The magnitude of axial velocities in the vortex illustrates the increasing strength of flow mixing with time and Reynolds number. The Steady state results of drag coefficient, angle of separation and length of the recirculation region compare very well with those obtained by different numerical methods in previous works.

2-Mathematical formulation

2.1 governing equations

The governing equations for the present purpose are the equations of conservation of mass (continuity) and momentum (Navier-Stokes), they are written in vector form with dimensionless variables as:

$$div\vec{V} = 0 \qquad (1)$$

$$\frac{Re}{2}\left(\frac{\partial \vec{V}}{\partial t} + \overrightarrow{rot}\,\vec{V}X\vec{V} + \overrightarrow{grad}\,\frac{V^2}{2}\right) = \Delta\vec{V} - \overrightarrow{grad}\,\hat{p} \qquad (2)$$

In this simulation the velocity vector $\vec{V}$ has two components $V_r(r,\theta)$ and $V_\theta(r,\theta)$, $\hat{p} = p + \rho g z$ where p is the static pressure and ρ the fluid density , g the gravitational acceleration ad z is the height . $Re = 2aV_\infty/\nu$, is the Reynolds number based on the sphere diameter 2a, twice the radius a; the velocity of the fluid far from the sphere V_∞ and ν is the kinematic viscosity .We used in equations (1) and (2) the dimensionless variables defined as : $r = r^*/a$; $V_r = V_r^*/V_\infty$; $V_\theta = V_\theta^*/V_\infty$; $t = t^*V_\infty/a$; $\hat{p} = \hat{p}^*/\rho V_\infty^2$; the asterisk indicates the dimensional variables.

Equations (1) and (2) are applied on the domain $1 \le r \le (r_\infty/a) and\ 0 \le \theta \le \pi$ accompanied with the boundary conditions which are: the no slip condition on the surface of the sphere , $r = 1, V_r = V_\theta = 0$ and the uniformity of the flow far from the obstacle, $r = {}^{r_\infty}/_{a}$, $V_r = cos\theta\ and\ V_\theta = -sin\theta$.

In addition we get the axisymetric hypothesis of the flow around the sphere.

First of all the unsteady Navier-Stokes equations are rewritten in vorticity and stream function formulation. We have used, for this purpose, the coordinate transformation $\xi = \ln(r)$ to refine the mesh in the vicinity of the sphere, where gradients may be important, without increasing the number of nodes, otherwise in the angular direction we change only the name of the variable $\eta = \theta$, the transformed domain is then $\xi \in \{1, \xi_\infty\}\ and\ \ \eta \in \{0, \pi\}$.

The numerical methodology begins with the first equation (1), it's used to define the stream function we have:

$$V_\xi = \frac{e^{-2\xi}}{\sin\eta}\frac{\partial\psi}{\partial\eta} \ ; \ V_\eta = -\frac{e^{-\xi}}{\sin\eta}\frac{\partial\psi}{\partial\xi} \qquad (3)$$

Equation (2) is transformed from it's original form when we take it's rotational, the term of pression get out and we have:

$$e^{\xi}\frac{\partial\omega}{\partial t} + V_\xi\frac{\partial\omega}{\partial\xi} + V_\eta\frac{\partial\omega}{\partial\theta} - \left(V_\xi + V_\eta\cot\eta\right)\omega = \frac{2}{\mathrm{Re}}e^{-\xi}\left(D^2\omega - \frac{\omega}{\sin^2\eta}\right)$$

D^2 is a differential operator

$$D^2 = \frac{\partial^2}{\partial\xi^2} + \frac{\partial}{\partial\xi} + \cot\eta\frac{\partial}{\partial\eta} + \frac{\partial^2}{\partial\eta^2} \qquad (4)$$

Otherwise the definition $\vec{\omega} = \overrightarrow{rot}\vec{V}$ is developped in spherical coordinates then the velocity components are replaced with the first derivatives of the stream function defined from the continuity equation

$$e^{3\xi} sin\eta.\omega = \frac{\partial \psi}{\partial \xi} - \frac{\partial^2 \psi}{\partial \xi^2} + cot\eta.\frac{\partial \psi}{\partial \eta} - \frac{\partial^2 \psi}{\partial \eta^2} \qquad (4)$$

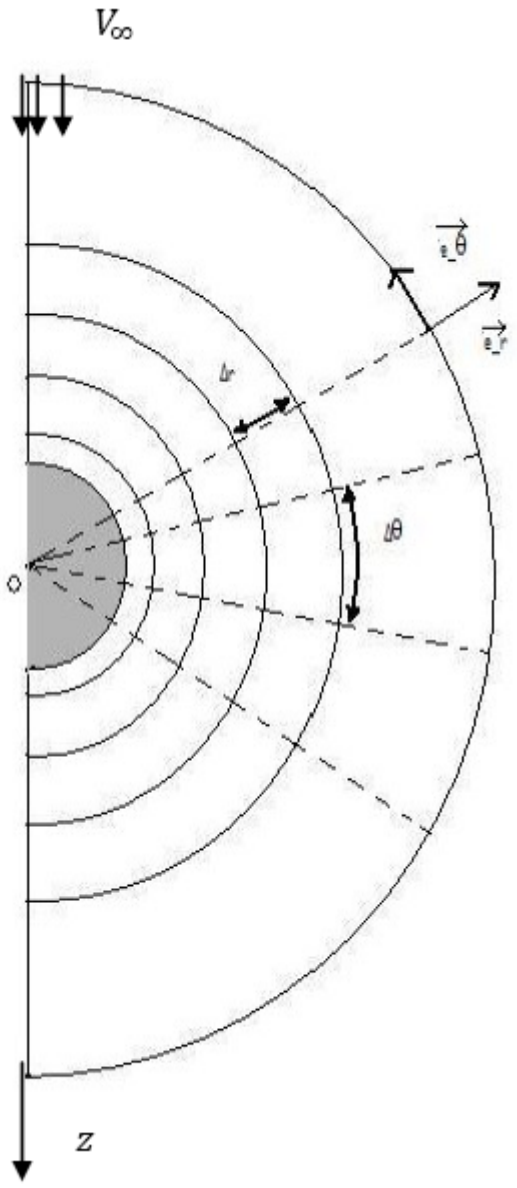

Figure 1 schematic spatial domain

Each point of the transformed domain $[0 \le \xi \le \xi_\infty\ ,\ 0 \le \eta \le \pi]$ is specified by it's indices:

$\xi_i = (i-1)\Delta\xi$ and $\eta_j = (j-1)\Delta\eta$ with $i = 1, \dots, NI$ and $j = 1, \dots, NJ$

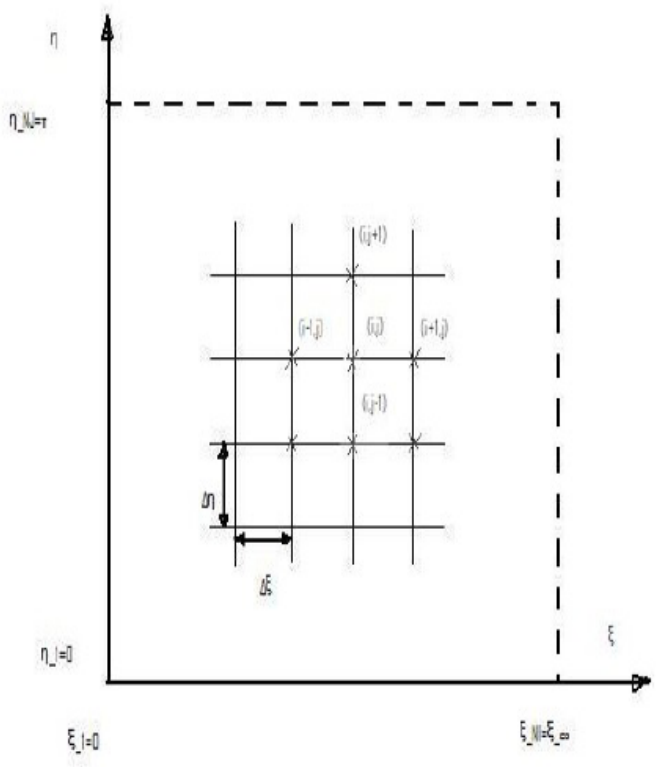

Figure 2 transformed domain mesh

2.2 Initial and boundary conditions

Since the simulation is concerned with an impulsively started movement, all dependant variables are equal to zero at initial time $t = 0$.

Otherwise the boundary conditions of the problem are translated in terms of the variables ω; ψ and the derivatives of . Therefore, we can write on the sphere $(\xi = 0)$

$$\psi(0,\eta) = 0 \quad and \quad \frac{\partial \psi}{\partial \xi}(0,\eta) = \frac{\partial \psi}{\partial \eta}(0,\eta) = 0$$

$$\frac{\partial^2 \psi}{\partial \xi^2}(0,\theta) = -\sin\eta.\omega(0,\eta) \quad \text{from equation (4)}$$

for surface conditions on the vorticity, we have drawn a relation from the fourth order Taylor expansion of the stream function ψ using only the first two nodes in the radial direction ξ; after that derivatives of ψ are replaced and then we obtain:

$$\omega(0,\theta).(2+4\Delta\xi) + \omega(\Delta\xi,\eta) = \frac{-6}{\sin\eta.\Delta\xi^2}.(\psi(\Delta\xi,\eta) - \psi(0,\eta)) \qquad (5)$$

The conditions far from the sphere are those of an irrotational flow, so they are expressed for t ≥ 0 as:
$\omega(\xi_\infty,\eta)=0$ and $\psi(\xi_\infty,\eta)=\frac{1}{2}e^{2\xi_\infty}sin^2\eta$

The first and second partial derivatives of $\psi(\xi,\eta)$ can be easily derived from $0.5e^{2\xi}sin^2\eta$.
The axisymetric hypotheses enforce the conditions

$\omega(\xi,0)=0=\omega(\xi,\pi)$
$\psi(\xi,0)=0=\psi(\xi,\pi)$
$\psi\eta\eta\ is\ an\ even\ function$

3-Methodology of resolution

The numerical method used in our simulation is presented for the first time in Bontoux (1978) and has proven its efficiency to simulate the flow over an impulsively started cylinder (Ta Phuoc Loc (1980), Ta Phuoc Loc and Bouard (1985). We have extended the use of this method for the study of the viscous flow over a sphere at moderate and high Reynolds numbers (Benabbas (1987)).
Because of the absence of boundary conditions on the rotational derivatives, the transport of rotational equation is not treated by the compact scheme. And it's the stream function equation witch benefits from enough conditions on all derivatives . So the use of Hermitian compact for equation (8) accompanied with the closure relations from the Merhstellen method [Cf. benabbas], for the derivatives $\psi\xi,\ \psi\xi\xi,\ \psi\eta\eta\ and\ \psi\eta\eta$:
Equation (8) is rewritten in an pseudo unsteady form and we use Optimum convergence coefficients $\lambda_{kh}\ et\ \lambda_{kv}$ of WASCHPRESS [cf. benabbas] they are calculated for 2^N iterations.

$$\frac{\partial\psi}{\partial\tau}_{i,j}+\psi\xi_{i,j}-\psi\xi\xi_{i,j}+cot\eta_j\psi\eta_{i,j}-\psi\eta\eta_{i,j}=e^{2\xi_i}sin\eta_j\omega_{i,j} \qquad (6)$$

For each iteration, equation (9) is discretised relative to only one direction so
in radial direction we have:

$$\lambda_{kh}\psi_{ij}^{p+\frac{1}{2}}+\psi\xi_{ij}^{p+\frac{1}{2}}-\psi\xi\xi_{ij}^{p+\frac{1}{2}}=(\lambda_{kh}\psi-cot\eta\psi\eta+\psi\eta\eta)_{ij}^{p}+e^{2\xi_i}sin\eta_j\omega_{ij}^{n} \qquad (7)$$

$$\frac{3}{\Delta\xi}(\psi_{i+1,j}-\psi_{i-1,j})-(\psi\xi_{i+1,j}+4\psi\xi_{i,j}+\psi\xi_{i-1,j})=0$$

$$\frac{12}{\Delta\xi^2}(\psi_{i+1,j}-2\psi_{i,j}+\psi_{i-1,j})-(\psi\xi\xi_{i+1,j}+10\psi\xi\xi_{i,j}+\psi\xi\xi_{i-1,j})=0$$

With the boundary conditions
$\psi_{1,j}=\psi\xi_{1,j}=0$
$\psi\xi\xi_{1,j}=-\sin\eta_j\quad\omega_{1,j}$
$\psi_{NI,j}=\frac{1}{2}e^{2\xi_{NI}}sin^2\eta_j$
$\psi\xi_{NI,j}=2\psi_{NI,j}\ ;\ \psi\xi\xi_{NI,j}=4\psi_{NI,j}$

And in angular direction we have

$$\lambda_{kv}\psi_{ij}^{p+1}+cot\eta_j\psi\eta_{ij}^{p+1}-\psi\eta\eta_{ij}^{p+1}=(\lambda_{kv}\psi-\psi\xi+\psi\xi\xi)_{ij}^{p+1/2}-e^{2\xi_i}sin\eta_j\omega_{ij}^{n}$$

$$\frac{3}{\Delta\eta}(\psi_{i,j+1}-\psi_{i,j-1})-(\psi\eta_{i,j+1}+4\psi\eta_{i,j}+\psi\eta_{i,j-1})=0$$
$$\frac{12}{\Delta\eta^2}(\psi_{i,j+1}-2\psi_{i,j}+\psi_{i,j-1})-(\psi\eta\eta_{i,j+1}+10\psi\eta\eta_{i,j}+\psi\eta\eta_{i,j-1})=0$$

With bounady conditions :
$\psi_{i,1}=\psi\eta_{i,1}=0$
$\psi\eta\eta_{i,1}\ est\ une\ \ fonction\ paire$
$\psi_{i,NJ}=\psi\eta_{i,NJ}=0$
$\psi\eta\eta_{i,NJ}\ \ est\ une\ fonction\ paire$
Regarding to the transport equation, The Peaceman – Rachford A.D.I. scheme is applied to the vorticity transport equation (6). The temporal evolution from $t\ to\ t+\Delta t$ is calculated in two steps, first of all $from\ t\ to\ t+\frac{\Delta t}{2}$ $then\ from\ t+\frac{\Delta t}{2}\ to\ \ t+\Delta t$, we have
First step of the resolution:
In the angular direction η equation (6) :

$$e^{\xi}\left(\frac{\partial\omega}{\partial t}\right)^{n+\frac{1}{2}}+V_\eta^n(\omega\eta)^{n+\frac{1}{2}}-(V_\xi+V_\eta\cot\eta)^n\omega^*-\frac{2}{Re}e^{-\xi}\left(\cot\eta\omega^{n+\frac{1}{2}}+\omega\eta\eta^{n+\frac{1}{2}}\right)=\frac{2}{Re}e^{-\xi}\left(\omega\xi\xi^n+\omega\xi^n-\frac{\omega^n}{sin^2\eta}\right)-V_\xi^n\ \ \omega\xi^n$$

ω^* will correspond to either ω^{n+1} or $\omega^{n+1/2}$ depending on whether the term $(V_\xi+V_\eta\cot\eta)$ has positive or negative value, in order to reinforce the principal diagonal.

Resulting in the tridiagonal equations :
$A_1\omega_{i,j-1}^{n+1/2}+B_1\omega_{i,j}^{n+1/2}+C_1\omega_{i,j+1}^{n+1/2}=D_1$
$for\ j=2,\dots,NJ-1$
With the conditions $\omega_1=\omega_{NJ}=0$
And in the second time step:

$$e^{\xi}\left(\frac{\partial\omega}{\partial t}\right)^{n+1}+V_\xi^n(\omega\xi)^{n+1}-(V_\xi+V_\eta\cot\eta)^n\omega^*-\frac{2}{Re}e^{-\xi}(\omega\xi\xi+\omega\xi)^{n+1}=\frac{2}{Re}e^{-\xi}\left(cot\eta.\omega\eta^{n+1/2}+\omega\eta\eta^{n+1/2}-\frac{\omega^n}{sin^2\eta}\right)-V_\eta^n\ \ \omega\eta^{n+1/2}$$

Then we develop $\omega\xi\ and\ \omega\xi\xi$ and then gather identical multiplier terms to get
$A_2\omega_{i-1,j}^{n+1}+B_2\omega_{i,j}^{n+1}+C_2\omega_{i+1,j}^{n+1}=D_2$
$for\ i=2,\dots,NI-1$
Completed With the discretisation of parietal condition on the rotational (10)

$$\omega_{1,j}(2+4\Delta\xi)+\omega_{2,j}=\frac{-6}{sin\eta_j\Delta\xi^2}(\psi_{2,j}-\psi_{1,j})$$

And the irrotational flow far from the sphere :

$\omega_{NI,1} = 0$

The method combines two numerical schemes. The classical ADI scheme is used to resolve the transport equation of the vorticity and the other, based on a compact hermitian method, is applied to the Poisson equation of the stream function (Benabbas (1987) for the details). This equation is treated as a parabolic one with the introduction of a pseudo-time and optimum coefficients of convergence are used in the iterative calculations.

In each direction (ξ and η) new dependant variables are taken into account :

$\psi, \frac{\partial \psi}{\partial \xi} and \frac{\partial^2 \psi}{\partial \xi^2}$ for the first half time step and

$\psi, \frac{\partial \psi}{\partial \eta} and \frac{\partial^2 \psi}{\partial \eta^2}$ for the second half time step.

The steady state is determined with a test on the vorticity field $\left|\omega^{n+1} - \omega^{n}\right| \leq \varepsilon = 10^{-4}$.

3-Results and discussion

3.1 steady state flow characteristics

Time evolution of the laminar separated flow past an impulsively started sphere has been calculated for various Reynolds numbers in the range of 20 to 1000. Before presenting transient dynamic behavior of the flow field, we would like to illustrate the efficiency of the numerical method used by presenting comparisons of our calculations for some important steady state characteristics with published experimental data and simulation results based on different numerical methods.

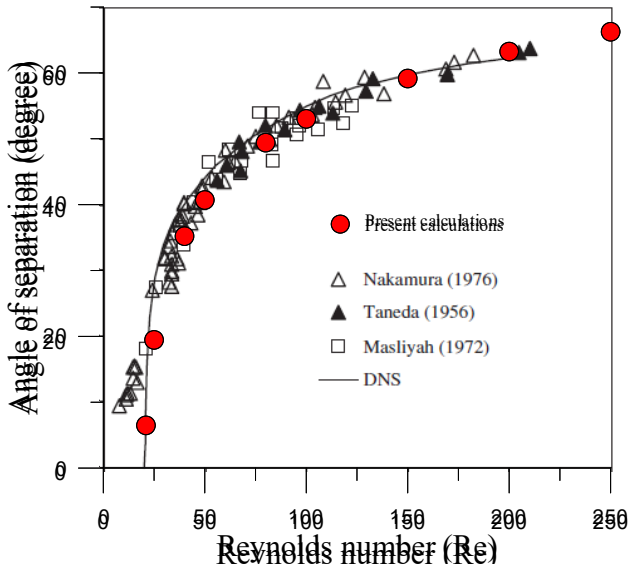

Fig.3: steady state angle of separation

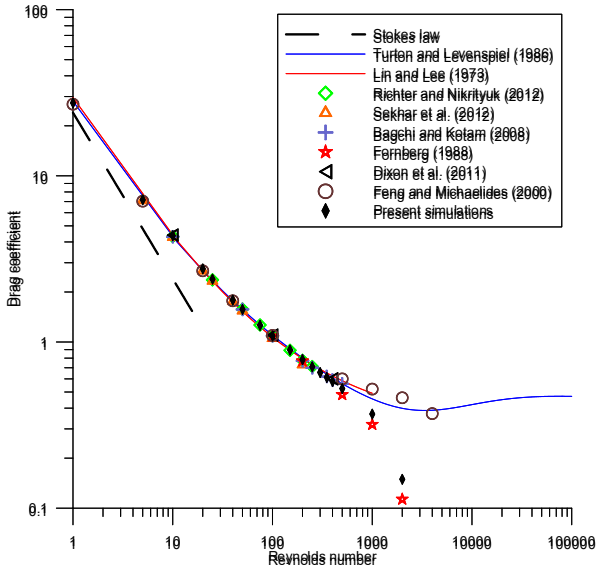

Fig.4: steady state drag coefficient

Figure 3 compares results of the angle of separation and shows very good agreement between practically all the data for the Reynolds numbers considered. The drag coefficient is presented in figure 4 and indicates an excellent agreement with experimental correlations and numerical results of different authors up to Reynolds number of 500. But for higher Reynolds numbers our calculations are close to those of Fornberg (1988) than the simulations of Feng and Michaelides (2001). The vortex length is reported in figure 5 and compared with experimental and numerical data. We observe a satisfactory agreement between them. The DNS results on figures 3 and 5 are of Reddy et al. (2010).

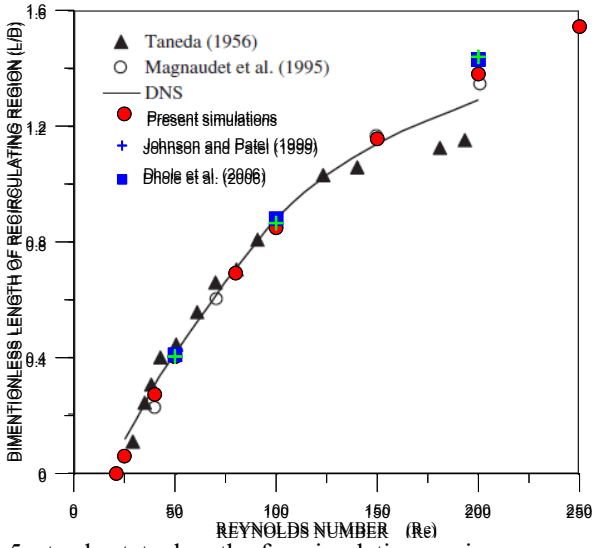

Fig.5: steady state length of recirculation region

All the above confrontations comfort the efficiency and accuracy of the numerical method used in the present study.

3.2 transient flow characteristics

Figures 6 and 7 show the vorticity at the surface of the sphere with time for Reynolds number respectively equal to 300 and 1000. The early stages of the flow are characterized by a fast growth of the recirculation region before reaching a slow development towards the steady state.

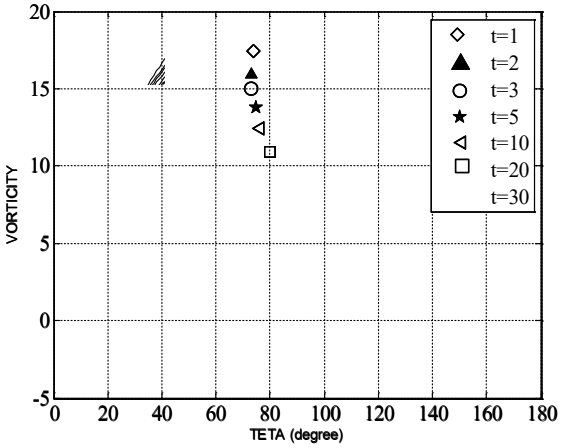

Fig.6: vorticity on the sphere at Re=300

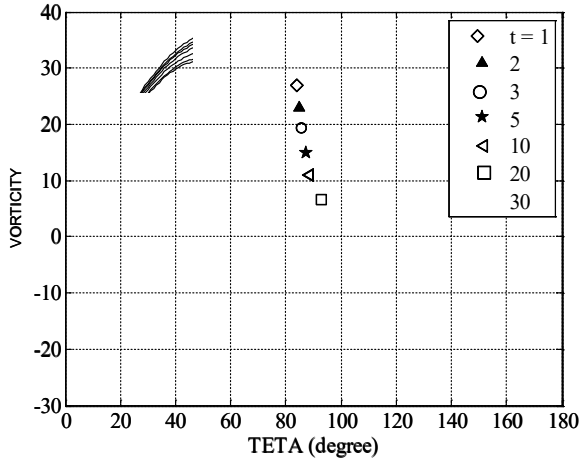

Fig.7: vorticity on the sphere at Re=1000

The sign change of the vorticity observed for Reynolds number of 1000 and time about t=5 indicates the birth of a secondary vortex of weak strength which has opposite rotation to the main vortex. This happens when the back flow itself separates from the sphere. The Reynolds number for which this phenomenon appears first is found to be 610.

In the case of a cylinder and for Reynolds number of 1000 two secondary vortices are observed (Ta Phuoc Loc (1980), Bouard and Coutanceau (1980)).

Figure 8 shows forward separation angle versus time for increasing Reynolds number. At early times the separation point moves at a rapid rate but then slowly approaches its steady state value. The transient length of the vortex behind the sphere for the same Reynolds numbers is reported on figure 7.

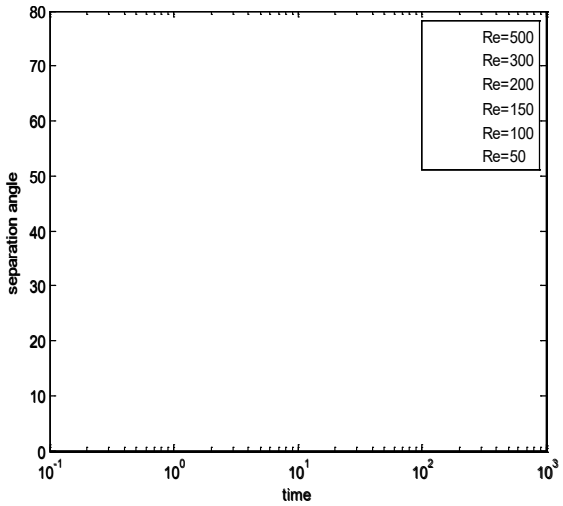

Fig.8: time evolution of separation angle

At the early stages the vortex grows rapidly in size and then followed by a slow approach to its final steady state value. The calculated steady state vortex lengths compare very well with values reported in other numerical and experimental studies as shown above (fig.5).

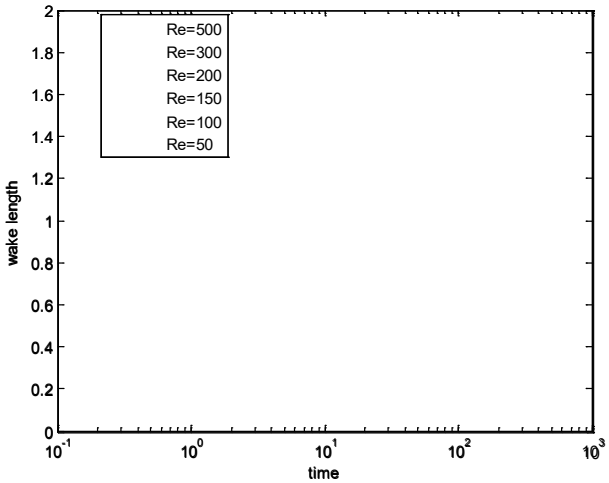

Fig.9: time evolution of vortex length

Figures 10 and 11 illustrate time evolution of the axial velocity on the axis of symmetry behind the sphere for Reynolds numbers of 300 and 1000. We can observe the increasing of the velocity modulus in the vortex region with time and Reynolds number but is limited to values lower than one. In the case of a cylinder, values higher than one are calculated (Ta Phuoc Loc (1980)). The growth of the velocity modulus with time illustrates the action of the convective mixing in the vortex. This action becomes stronger with increasing Reynolds number.

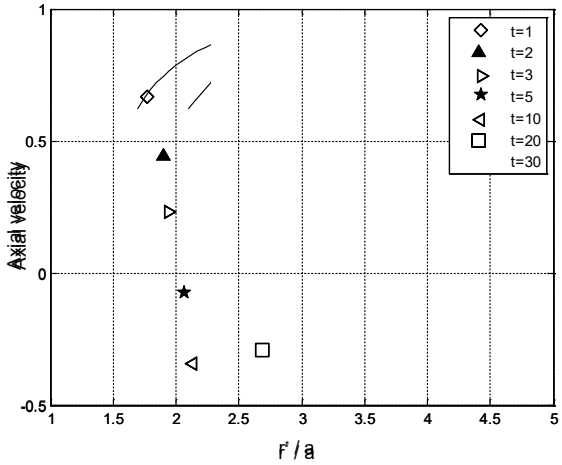

Fig.10: time variation of axial velocity at Re=300

The null value of the velocity on the axis indicates the limit of the vortex region and so its length. For the same time, the vortex length is slightly higher for Re=300 than for Re=1000.

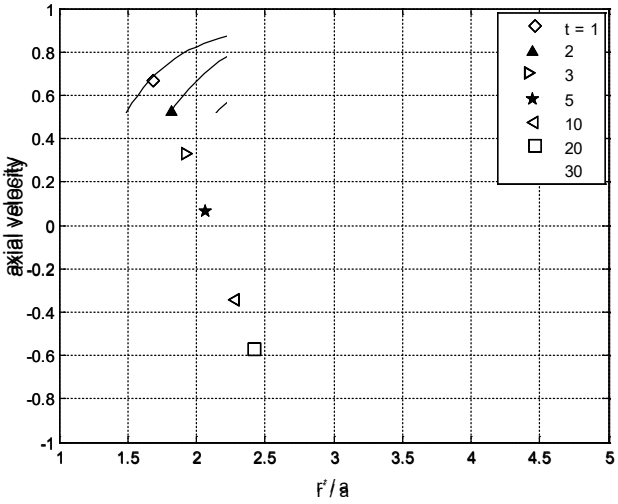

Fig.11: time variation of axial velocity at Re=1000

CONCLUSION

The complex problem of the transient laminar separated flow over an impulsively started sphere has been conducted with efficient mixed hermitian compact method. The steady state results have been successfully compared to the highest accurate methods used till now. The transient characteristics of the flow have concerned the vorticity on the sphere under the influence of Reynolds number and the results revealed the appearance of secondary vortex at Reynolds number of 610. Time evolution of the separation angle and the vortex length are also presented and the simulations have shown a rapid growth of these characteristics at the early stages of the flow development. The transient behavior of axial velocity behind the sphere indicated how the convective mixing in the vortex increases with time and Reynolds number. The present results constitute a valuable basis to understand the enhancement of heat and mass transfer in cyclic regime of fluidized or fixed beds.

REFERENCES

1. Bagchi P., Kottam K., 2008. Effect of free stream isotropic turbulence on heat transfer from sphere. Phys. Fluids. 20, 073305.
2. Bontoux P., 1978. Contribution à l'étude des écoulements visqueux en milieu confiné. Analyse et Optimisation de méthodes numériques de haute précision. Thèse de Doctorat ès-sciences, Université d'Aix-Marseille II, France.
3. Benabbas F. ,1987. Etude numérique de l'écoulement autour d'une sphère aux grands nombres de Reynolds en régime stationnaire et instationnaire. Thèse de Doctorat de Troisième cycle. Université de Poitier, France.
4. Benabbas F., Brahimi M., Tighzert H. , 2003. Caractérisation du très proche sillage d'une sphere à des nombres de Reynolds modérés et spectres singuliers . "16ième Congrès Français de Mécanique." , Nice, France, Sep. 1–5, pp. 1–7.
5. Benabbas F., Brahimi M., 2012. Transient mass transfer around an impulsively started spherical particle at low to high Peclet numbers. "The 9th EuroMech Fluid Mech. Conf.", Rome, Italy, Sep. 9-13, accepted.
6. Bouard R., Coutanceau M., 1980. The early stage of development of the wake behind an impulsively started cylinder for $40 \leq Re \leq 10^4$. J. Fluid Mech. 101, 583-607

7. Collins W. M., Dennis S .C. R., 1973. Flow past an impulsively started circular cylinder. J. Fluid. Mech., 60,105-127.

8. Dhole S. D., Chhabra R. P., Eswaran V., 2006. A numerical study on the forced convection heat transfer from an isothermal and isoflux sphere in the steady symmetric flow regime. Int. J. heat and mass transfer. 49, 984-994.
9. Dixon A. G., Taskin M. E., Nijemesisland M., Stitt E. H., 2011. Systematic mesh development for 3D CFD simulation of fixed beds: Single sphere study. Comp. Chem. Eng., 35, 1171-1185.
10. Fornberg B., 1988. Steady viscous flow past a sphere at high Reynolds numbers. J. Fluid Mech.190, 471-489.
11. Feng Z., Michaelides E. E., 2000. A numerical study on transient heat transfer from a sphere at high Reynolds and Peclet numbers. Int. J. Heat and Mass transfer. 43, 219-229.
12. Gushchin V. A., Matyushin R. V., 2006. Vortex formation mechanisms in the wake behind a sphere for $200 \leq Re \leq 380$. Fluid Dyn. 41,N°5,795-809.
13. Johnson T. A., Patel V. C. (1999). Flow past a sphere up to a Reynolds number of 300. J. Fluid Mech. 378, 19-70.
14. Kechroud N., Brahimi M., Djati A. (2010a). Characterization of dynamic behavior of the continuous phase in liquid fluidized bed. Powder Tech., 200, issue 3, 149-157.
15. Kechroud N., Brahimi M., Djati A. (2010b). Spectral analysis of dynamic behavior of the continuous phase in liquid fluidized bed. " Proc. of 7th Int. Conf. on Multiphase Flow .," Tampa Fl, USA, May 30 –June 4, pp.1-7
16. Lee S., (2000). A numerical study of the unsteady wake behind a sphere in a uniform flow at moderate Reynolds numbers. Comp. Fluids, 29,639-667.
17. Lin C. L., Lee S. C., (1973). Transient state analysis of separated flow around a sphere. Comp. Fluids, 1,235-250.
18. Magnaudet J., Rivero M.,Fabre J., (1995). Flows past a rigid sphere or a spherical bubble.1. steady straining flow. J. Fluid Mech., 284, 97-135.
19. Masliyah J. H., (1972). Steady wakes behind oblate spheroids: flow visualization. Physics of fluids 16, 6-8.
20. Nakamura, I., (1976). Steady wake behind a sphere. Physics of fluids. 19, 5-8.
21. Reddy R. K., Joshi J. B., Nandakumar K., Minev P. D., (2010). Direct numerical simulations of a freely falling sphere using fictitious domain method: Breaking of axisymmetric wake. Chem. Eng. Sc.,65, 2159-2171
22. Richter A., Nikrityuk P. A., (2012). Drag forces and heat transfer coefficients for spherical, cuboidal and ellipsoidal particles in cross flow at sub-critical Reynolds numbers.Int. J. heat and mass transfer,55, 1343-1354
23. Rimon Y., Cheng J., (1969). Numerical solution of a uniform flow over a sphere at intermediate Reynolds numbers. Phys. Fluids 12, N°5, 949-959
24. Sekhar T. V. S., Hema Sundar Raju B., (2012). Higher-Order compact scheme for the incompressible Navier-Stokes equations in spherical geometry,Commun. Comput. Phys., 11, N°1, 99—113.
25. Smith P. A., Stansby P. K., (1988). Impulsively started flow around a circular cylinder by the vortex method. J. Fluid Mech., 194, 45-77.
26. Taneda S.,(1956). Experimental investigation of the wake behind a sphere at low Reynolds numbers. Journal of the physical society of Japan, 11, 1104-1108.
27. Ta Phuoc Loc, Bouard R., (1985). Numerical solution of the early stage of the unsteady viscous flow around a circular cylinder: a comparison with experimental visualization and measurements. J. Fluid Mech., 160, 93-117.
28. Ta Phuoc Loc, (1980). Numerical analysis of unsteady secondary vortices generated by an impulsively started circular cylinder. J. Fluid Mech., 100,111-128.
28. Thoman D. C., Szewczyk A. A., (1969). Time-dependant viscous flow over a circular cylinder. Phys. Fluids Suppl., 12, 76-87.
29. Turton R., Levenspiel O., (1986). A short note on the drag correlation for spheres. Powd. Tech.47, 83-86.

UNGRAVITY AND APPLICATIONS

N. MEBARKI

Laboratoire de Physique Mathematique et Subatomique, Physics Department, Faculty of Fundamental Sciences, Frères Mentouri University, Constantine, Algeria.

Reçu le 12/08/2014 – Accepté le 21/11/2015

Abstract

A model based on the ungravity proposal is presented. Some applications explaining dark energy and dark matter are discussed.

Keywords: Cosmic magnetic field, redshift, gravitational waves, cosmological observation.

Résumé

Un modèle se basant sur une proposition de la ungravitation est présenté. Quelques applications expliquant énergie et matière noires ont été discutées.

Mots clés : Champ magnétique cosmique, décalage vers le rouge, ondes gravitationnelles, observation cosmologique.

ملخص

نموذج يعتمد على فرضية اللاتجاذب و أقترح بعض التطبيقات تفسر الطاقة المظلمة والمادة السوداء نوقشت.

الكلمات المفتاحية : الحقل المغناطيسي الكوني،الإنزياح نحو الأحمر، الأمواج الجاذبية، المشاهدة الكسمولوجية.

I. INTRODUCTION

From Hubble's observations of galaxies recession, the redshift of galaxies has made a revolution in our view to the universe. The Hubble law links two important quantities: the cosmological redshift and distance of the observed object (galaxies, quasars, or supernovae…). The distance recalibration has given more accurate determination of the cosmological distances and results a big change of Hubble Constant from 500km/s/Mpc as initial estimation, to around 70km/s/Mpc, the actual accepted value from the cosmic microwave background observations. This latter is one of the key parameters of the modern cosmology.

We investigate a new effect that can be in origin of supplementary redshift contributing with the one of cosmological origin to the total observed redshift of galaxies. Our aim in this work is to prove the origin and estimate the contribution and implications of this non cosmological redshift. This new redshift effect does not result from the universe expansion or the peculiar motion of galaxies. It is due to the photon radiation of high frequency gravitational waves in an external magnetic field. The estimation of this effect on the total observed redshift will serve as another recalibration of the cosmological parameters improving our understanding to the universe.

The following sections are organized as follow: the next section present the methodology to follow; after that, a section to give the results on the non cosmological redshift contribution; then, one for the foundation and argumentation to compare with previous works; finally, discussion and conclusion section to suggest some possible evidence and observational contaminations with this new non cosmological redshift. We take the convention on units as: (c, κ, μ_0) representing the speed of light, gravitational constant of Einstein equations and the Permeability of the vacuum respectively.

II. METHODOLOGY: COMPUTE THE REDSHIFT EFFECT

We are interested in the light propagation through spacetime and their gravitational interaction. In the Einstein theory of gravity, the energy momentum tensor part includes

the matter and electromagnetic fields contributions. We restrict the study to the vacuum case (absence of matter). The background is a flat spacetime represented by Minkowski metric($\eta_{\mu\nu}$). We treat the weak Linearized gravity [1-3] where the curvature caused by the energy of the electromagnetic waves will be small enough to be a perturbation given by ($h_{\mu\nu}$) in the first order approximation of the metric as in (1) and the Einstein equations will be as in eq.(2)..

$$g_{\mu\nu} = \eta_{\mu\nu} + h_{\mu\nu} \tag{1}$$

$$\partial_\alpha \partial^\alpha \bar{h}_{\mu\nu} + \eta_{\mu\nu}\partial_\alpha \partial_\beta \bar{h}^{\alpha\beta} - (\partial_\mu \partial_\alpha \bar{h}^{\alpha}{}_{\nu} + \partial_\nu \partial_\alpha \bar{h}^{\alpha}{}_{\mu}) = -2T_{\mu\nu} \tag{2}$$

Where $\bar{h}_{\mu\nu}$ is given by $\bar{h}_{\mu\nu} = h_{\mu\nu} - \frac{1}{2}\eta_{\mu\nu}h^{\alpha}_{\alpha}$. In vaccum and with the traceless transverse gauge as in (3), we define solutions of equations (2) as gravitational waves.

$$\begin{aligned} &\partial_\beta \bar{h}^{\alpha\beta} = 0, \\ &h_\alpha{}^\alpha = 0 \end{aligned} \tag{3}$$

We assign an energy-momentum tensor $t_{\mu\nu}$ to the gravitational field itself just as we do for electromagnetism, or any other field theory. Physically, we accept the gravitational radiation that will carry a part of energy-momentum just as any physical radiation does. In the weak Linearized gravity, this contribution can be shown in Einstein tensor as in (4) and (5) by considering the higher orders of the perturbation $h_{\mu\nu}$.

$$G_{\mu\nu} = G^{(1)}{}_{\mu\nu} + G^{(2)}{}_{\mu\nu} + G^{(3)}{}_{\mu\nu} + \ldots = -T_{\mu\nu} \tag{4}$$

$$t_{\mu\nu} = G^{(2)}{}_{\mu\nu} + G^{(3)}{}_{\mu\nu} + \ldots \tag{5}$$

We should, at each point in spacetime, average over a small region in order to probe the physical curvature. It is worth a good approximation to take the second order only. For a metric having the form in (1), the gauge invariant measure of the gravitational field will be given as in (6).

$$t_{\mu\nu} = \frac{1}{4}\left\langle \begin{aligned} &\partial_\mu \bar{h}_{\alpha\beta}\partial_\nu \bar{h}^{\alpha\beta} - 2\partial_\alpha \bar{h}^{\alpha\beta}\partial_{(\mu}\bar{h}_{\nu)\beta} \\ &-\frac{1}{2}\partial_\mu \bar{h}_\beta{}^\beta \partial_\nu \bar{h}_\alpha{}^\alpha \\ &-(4\bar{h}_{\alpha(\mu}T_{\nu)}{}^{\alpha} + \eta_{\mu\nu}h^{\alpha\beta}T_{\alpha\beta}) \end{aligned} \right\rangle \tag{6}$$

The energy carried by the physical gravitational waves is determined by the energy flux F in the propagation direction that is only the t_{0i} components of this energy momentum tensor. The energy loss computed with method for the binary pulsar was observed by Hulse and Taylor [4] for PSR1913+16 within an accuracy of 3%. These observations are the evidence of the gravitational waves and give a Nobel Prize to Hulse and Taylor in 1993.

When interested to the gravitational interactions of electromagnetic waves, the methodology to follow is: first, we compute the electromagnetic fields $F_{\mu\nu}$ energy momentum tensor as in (7), and then compute the solution to the weak Linearized gravity equations as in (2), after that accept solutions with non-vanishing energy momentum tensor of the radiated gravitational waves, finally compute the energy carried by these physically accepted radiations. The energy carried will be seen as a redshift in the electromagnetic wave frequency.

$$T_{\mu\nu} = -(F_{\mu\alpha}F_\nu{}^\alpha - \frac{1}{4}\eta_{\mu\nu}F_{\alpha\beta}F^{\alpha\beta}) \tag{7}$$

III. NON COSMOLOGICAL REDSHIFT EFFECT

Following the steps described previously, we have computed three possible situations. First, plane transverse electromagnetic waves have vanishing energy momentum tensor even for higher orders. Then, plane electromagnetic waves in a transverse magnetic (or electric) mode have non vanishing energy momentum tensor. This situation is more likely to find in electromagnetic waves propagating in a medium. Finally, monochromatic plane transverse electromagnetic waves propagating in the presence of external magnetic fields have a non vanishing energy momentum tensor. This situation can be found in a cosmological context.

Dealing with Minkowski space described by Cartesian coordinates, the external transverse magnetic field $\vec{B}_{ext} = (B_x, B_y, 0)$ will be static, homogenous and extend in a restricted spatial area where (L) represents the coherent length of the magnetic fields. The electromagnetic wave is considered to propagate in the z-direction from $(-\infty)$.The electric and magnetic vectors are $\vec{E}_{photon} = (E_0 cos(k(t - z)),0,0)$ and $\vec{B}_{photon} = (0, B_0 cos(k(t - z)),0)$ where the wave number is $(k = 2\pi\nu)$and $(B_0 = E_0)$ and the photon frequency is (ν). The radiative energy momentum tensor of these electromagnetic fields is only the intersection part of the type fields.

The space of propagation can be decomposed to three parts; the first and the third parts with no magnetic fields and the second where the electromagnetic waves will radiate gravitational waves losing energy in this process. To find this loss in energy, we first solve the equations (2) in the three parts, respecting the continuity condition (8), and then follow the other steps of our methodology.

$$\begin{aligned} &\bar{h}_{\mu\nu}{}^{(I)}(z=0) = \bar{h}_{\mu\nu}{}^{(II)}(z=0); \\ &\bar{h}_{\mu\nu}{}^{(II)}(z=L) = \bar{h}_{\mu\nu}{}^{(III)}(z=L) \end{aligned} \tag{8}$$

The energy momentum tensor, for the out-going gravitational radiations in the third part, has non-vanishing components, as given in (9), for light waves propagating in an external magnetic field.

$$t_{00} = -t_{03} = \frac{E_0^2 z^2}{4}(B_X^2 + B_Y^2) \tag{9}$$

To determine the loss of photon's energy E, we consider the energy flux F in the propagation direction that can be given by (10).

$$F = \frac{-dE}{d\Omega dt} = -t^{0i} n_i \qquad (10)$$

Where: $(d\boldsymbol{\Omega dt})$ represent the variation in time and in the surface perpendicular to the direction of propagation. We set up a new non expansion part of the observed redshift on our result derived from the energy loss due to the gravitational radiation in an external magnetic field from photons. The relation of the non cosmological redshift (z_{NC}), as in (11), will be exponentially proportional to the transverse external magnetic field strength $B_\perp = \sqrt{B_x^2 + B_y^2}$ and coherent length (L).

$$1 + z_{NC} = \exp(\frac{1}{12} B_\perp^2 L^3) \qquad (11)$$

The new non expansion part of the redshift must be considered from the widespread magnetic field of galaxies, clusters, filaments in large scale structure [5-6]. The magnetic fields in the universe has take ample evidence in a wide variety of scales and magnitudes: galactic ranges with strength 1μG and coherent length of few kpc, clusters ranges with 1-10μG and coherent length 10-100kpc and filaments ranges with 0.3μG and coherent length 1Mpc. This proved redshift has a significant amount for the magnetic field that has, as an average, strength of 1μG that spread on a coherence length of 100kpc. The magnitude of the redshift zNC for cosmic magnetic fields will be 13.45×10^{-3} and grow when the field is stronger or have more coherence length. The spacetime curvature of Schwarzschild spacetime will also contribute to our redshift as given in (12) as a first approximation to the situation.

$$1 + z_{NC} = \exp[\frac{1}{4} B_\perp^2 (\frac{1}{3} L^3 + mL^2 + 4m^2 L + 8m^3 \ln[|1 - 2m|/(2m)])] \qquad (12)$$

Our amplifier redshift depends on some fundamental properties of galaxies and clusters. These three parameters are the magnetic field strength(B), the effective spatial spread or the coherence length (L) and the total mass of galaxies or clusters (m) included in the total mass of the luminous object causing the spacetime curvature. We have to associate the two redshifts in the global observed redshift $(z_{observed})$, as given in (13), as done by many authors [7].

$$1 + z_{observed} = (1 + z_C)(1 + z_{NC}) \qquad (13)$$

(z_C) is the cosmological redshift due to the expansion and (z_{NC}) is the non cosmological redshift or the non expansion origin such as our redshift. This new redshift effect will be like an amplifier of the observed cosmological redshift of galaxies due to their own magnetic field or for galaxies in clusters of filaments by the intergalactic magnetic field.

IV. FOUNDATION AND ARGUMENTS

The propagation of electromagnetic waves in external magnetic fields is studied previously and referred as Gertsenshtein effect. In some works [8-16], the Gertsenshtein effect and its inverse are viewed as processes of photon graviton conversion. They have used some probability $P = 4\pi G B^2 L^2$ of conversion depending on the external magnetic field and its coherence length. The photon graviton conversion has been explored as a possible mean to generate the observed anisotropies of the cosmic microwave background. Cillis and Harrari [17] estimate the faint possibility of conversion that will tend to be smaller in the existence of plasma. The plasma will make the probability depending to the photon frequency and so cannot produce detectable anisotropies in the cosmic microwave background. Ejlli [18] present a new paper in the same subject. Pshirkov and Baskaran [19], contrarily to the previous view and in the presence of a strong enough high frequency gravitational wave background, significant anisotropies in the microwave background will be produced by the inverse Gertsenshtein effect.

The non cosmological redshift effect is believed to clarify some misunderstanding done in the construction of the conversion view. First, The Einstein field equations and the electrodynamics equations in curved space time that describe the Gertsenshtein effect and its inverse are classical theories do not deal with quantums and we cannot deduce a conversion between the photon and the graviton. Second, the probability of conversion was a ratio between the carried energy and the initial energy of electromagnetic waves; representing more a transferred energy than a probability. Third, the non cosmological redshift is computed by the loss energy method that was in origin of the observations of Hulse and Taylor. For the special case of microwave background anisotropies, the high frequency gravitational waves background has no evidence of black body spectrum shape and their conversion to microwave photons will produce a random spectrum. The non cosmological redshift effect is believed to be more coherent and consistent with a method that give observed results.

V. DISCUSSION AND CONCLUSION

As an application, this effect can be an explanation of some anomalous redshift as a discordant behavior of our amplifier redshift such as: Stephan Quintet the compact interacting galaxy group, the galaxy-quasar associations and the discordant redshifts of some types of galaxies [20-21]. We have found that in all the above mentioned cases, a relation between these anomalous redshifts and the existence of strong sources of magnetic field supporting the nature of our non cosmological redshift.

Other implications are possible observational measurement contamination. Several models predict a primordial cosmic magnetic field from the inflation, given a possible primary and secondary CMB anisotropies can be from the non cosmological redshift origin. The redshift observations of the Supernovae SN Ia have to be amplified by this effect. These two possible observational measurement contaminations affect the cosmological parameters estimations through CMB and SN Ia measurements. The observational measurements of the cosmic magnetic field by the Faraday rotation [22], defined in (14) and (15), have to consider this effect and reconsider the actual measured magnetic fields and electron densities of galactic and

intergalactic medium.

$$RM(z_s) = 8.1\times10^5 \int_0^{z_s} n_e B_{||}(z)(1+z)^{-2}\, dl(z) \quad (14)$$

$$dl(z) = 10^{-6} H_0^{-1}(1+z)(1+\Omega z)^{-1/2}\, dz \quad (15)$$

Where: (z_s) source of light redshift, $(B_{||})$ longitudinal magnetic field and (n_e) electron density in the medium. The total observed redshift will be amplified compared to the case without magnetic fields in the line of sight trajectory. Due to this non cosmological redshift, objects in the existence of magnetic field will be apparently more distant. This effect on the distance of cosmic objects estimation is crucial in many fields of astrophysical study, such as the ultrahigh energy cosmic rays UHECR, Greisen–Zatsepin–Kuzmin cutoff [23] and the sources identification problem [24].

It is worth to mention that this non cosmological contribution will account for the recalibration of Hubble parameter and the dark matter content of galaxies and clusters.

Our preliminary results are qualitative and not quantitative (more studies are under investigations).

ACKNOWLEDGMENT

We are very grateful to the Algerian Ministry of education and research as well as the DGRSDT for the financial support

VI. REFERENCES

[1] I. Ciufolini, V. Gorini, U, Moschella, P. Fre "Gravitational Waves", *IOP Publishing* (2001).

[2] I. Ciufolini, R.A. Matzner, "General Relativity and John Archibald Wheeler", "Part III: Gravitational Waves", *Springer Science Press*, (2010).

[3] A. Krasinski, J. Plebanski, "An Introduction to General Relativity and Cosmology", *Cambridge University Press* 9780521856232 (2006).

[4] Hulse, Taylor, "An Introduction to General Relativity and Cosmology", *Astrophys. J. Lett*. 195, 151, (1975).

[5] M. Murgia, F. Govoni, L. Feretti, G. Giovannini, D. Dallacasa, R. Fanti, G. B. Taylor, and K. Dolag, "Magnetic Fields and Faraday Rotation in Clusters of Galaxies", *Astron.Astrophys*. 424 429-446 (2004) [DOI: 10.1051/0004-6361:20040191].

[6] H. A. Bonafede, L. Feretti, M. Murgia, F. Govoni, G. Giovannini, V. Vacca, "Galaxy cluster magnetic fields from radio polarized emission", Published in proceedings of "ISKAF2010 Science Meeting" [astro-ph/1009.1233v1].

[7] R. J. V. Narlikar, "Creation of Matter and Anomalous Redshifts", appear in the book of R.L. Amoroso, G. Hunter, M. Kafatos, J.P. Vigier, "Gravitation and Cosmology: From the HubbleRadius to the Planck Scale, Proceedings of a Symposium in Honour of the 80th Birthday of Jean-Pierre Vigier", Edited by *Kluwer Academic Publishers* 2003.

[8] G. M.E. Gertsenshtein, "Wave resonance of light and gravitational waves", *Soviet Physics JETP*, volume 14, number 1, 84-85 (1962).

[9] M. Gaspirini, V. de Sabbata, "Introduction to Gravitation*", World Scientific Publishing* (1985).

[10] R.A.Issason, "Gravitational Radiation in limit of High Frequency", *Phys.Rev.* 166 1263 (1968).

[11] L.P. Grishchuk, M.V. Sazhin, "Emission of gravitational waves by an electromagnetic cavity and detection", *Sov.Phys. JETP* 32 213 (1974).

[12] V.B. Braginsky and V.H. Rudenko, "Gravitational waves and the detection of gravitational radiation", Section 7:"Generation of gravitational waves in the laboratory", *Physics Report,* 46 Number 5, 165-200 (1978).

[13] S.W. Hawking, W. Israd,, "General Relativity: An Einstein Centenary Survoy", *Cambridge University Press* 90-137 (1979).

[14] P. Chen, "Resonant Photon Graviton Conversion in EM Fidas: From Earth to Heaven", *Stanford Linear Accelerator Center-PUB-6666* (Semptember 1994).

[15] R.M.L. Baker, G.V. Stephenson and F.Y.Li, "Proposed ultra-high sensivity HFGW Detector", in the Proccedings of the space Technology and Applications Int. Forum (STAIF-2008), *American Institute of Physics Conference Proceedings* 969 1045-1054 (2008).

[16] H. collins, "Gravity's Shadow", *University of Chicago Press* (2004).

[17] A.N. Cillis and D.D. Harari, "photon-graviton conversion in a primordial magnetic field and the cosmic microwave background", *Phys.Rev.D* 54 4757-4759(1996)DOI: 10/1103/ PhysRevD.54.4757.

[18] D. Ejlli, "Graiton production from the CMB in large scale magnetic fields", *Phys.Rev.D* 87 124029(2013) DOI: 10/1103/ PhysRevD.87.124029.

[19] M.S. Pshirkov, D. Baskaran, "limits on high frequency Gravitational Wave Background from its interplay with Large Scale Magnetic Fields", *Phys.Rev.D* 80 042002 (2009) DOI: 10/1103/ PhysRevD.80.042002.

[20] E. O'Sullivan, S. Giacintucci, J.M. Vrtilek, S. Raychaudhury, L.P. David, "A Chandra X-ray view of Stephan's Quintet: Shocks and Star-formation", *Astrophys.J* . 701 1560-1568 (2009).

[21] P. Galianni, E.M. Burbidge, H. Arp, V. Junkkarinen, G. Burbidge, S. Zibetti, "The Discovery of a High Redshift X-ray Emitting QSO Very Close to the Nucleus of NGC 7319", *Astrophys.J.* 620 88-94 (2005).

[22] D. Grasso, H.R. Rubinstein, *Physics Reports* 348 163,266 (2001).

[23] K. Greisen, *Phys. Rev. Lett*. 16, 748 (1966). G. T. Zatsepin, V.A. Kuzmin, Pisma Zh. *Experim. Theor. Phys.* 4, 114 (1966).

[24] R.U. Abbasi et al. [HiRes Collab.], *Phys. Rev. Lett*. 92, 151101 (2004). R. U. Abbasi et al. *Phys. Rev. Lett*. 100, 101101 (2008); arXiv:astro-ph/0703099. C.C.H. Jui [Telescope Array Collab.], arXiv:1110.0133. Y.Tsunesada [Telescope Array Collab.], arXiv:1111.2507. P.Abreu et al. [Pierre Auger Collab.], arXiv:1107.4809. F. Salamida [Pierre Auger Collab.], 32nd ICRC, Beijing, China, 2011. J.Abraham et al. [Pierre Auger Collab.], *Phys. Rev. Lett.* 104, 091101 (2010). J.A. Bellido et al [Pierre Auger Collab.],Proc. 31st ICRC Lodz 2009. L.Gazon, for the Pierre Auger Collaboration, *J.Phys.Conf.Ser*. 375 052003 (2012), arXiv:astro-ph/1201.6265

SOME VIABLE MODELS FOR EXTRA DIMENSIONAL UNIVERSE

A. MOHADI

Laboratoire de Physique Mathematique et Subatomique, Physics Department, Faculty of Fundamental Sciences, Frères Mentouri University, Constantine, Algeria.

Reçu le 12/05/2014 – Accepté le 24/06/2014

Abstract

Some viable models in a 5D space-time are presented and Friedman like equations are also obtained. A dynamical study is also investigated.

Keywords: ***Extra dimension, Dynamical study***

Résumé

Quelques modèles viables dans espace-temps a 5D ont été présentés et des équations du type Friedman ont été obtenues. Une étude dynamique a été aussi investie.

Mots clés : ***dimension supplémentaires, étude dynamique.***

ملخص

بعض النماذج الحيوية في فضاء زمكان ذو 05 أبعاد قد طرح ومعادلة فريدمان المناسبة قد استنتجت. دراسة ديناميكية قد استعملت.

الكلمات المفتاحية : بعد إضافي، دراسة ديناميكية.

I. INTRODUCTION

In 1919, Theodor Kaluza developed a fundamental description to unify the electromagnetism and gravitation forces by introducing extra-dimensions in General Relativity[1]. the Standard Model can not describe the gravitation because of its high energy scale (10^{15}Gev), which leads us to look for a new physics.

By using the fifth dimension and according to Kaluza-Klein, the start was with a pure five dimensional gravitation but all the fields have to be independents of this extra-dimension and they can be written as a function of four-dimensional fields where the Maxwell equations are hidden in Einstein equation.

In this case, Kaluza theory preserves the geometry of General Relativity but the electromagnetic fields are added as a vibration in the five-dimensional space.

In 1926, Oskar Klein succeeded to explain why we can not perceive the additional dimension. He has considered that the five-dimensional fields are independent from the extra-dimension, which must be compactified. This means that it has a topology of a circle. for example a cylinder with a radius of the order of Plank length (it is extremely small).

The recent observations indicate that our universe is in a large scale in accelerated expansion. This was first observed from high red shift supernova Ia [1 ,7], and confirmed later by cross checking from the cosmic microwave background radiation [8,9]. The expansion rate was explained in the cosmological standard model by adding dark energy , which has a negative pressure . However, the nature of dark energy as well as dark matter is yet unknown , as long as the solution is not yet obtained in the context of the standard General Relativity. This leads to suggest a five dimensional model. Mohammedi gives an alternative explanation to dark energy responsible for the accelerated expansion of the universe by incorporating extra dimensions into Friedmann-Robertson-Walker (FRW) cosmology [10].

In this paper, we concentrate on some cosmological models with just one extra dimension and look for exact solutions as well make a general dynamical study to understand the stability and behavior of the general solutions.

II. FRW UNIVERSE WITH ONE EXTRA DIMENSION

The metric of a 5D space-time with a 4D spherical symmetric universe, isotropic and homogenous has the following form [11]:

$$ds^2 = dt^2 - R^2(t)\left[\frac{dr^2}{1-kr^2} + r^2(d\theta^2 + sin^2\theta d\varphi^2)\right] - A^2(t)dy^2 \quad (1)$$

Where A(t) is a scale factor of the extra-dimension, y is the fifth coordinate, k=-1,0,1 depending on the type of the 3D space geometry. By using the metric F.R.W and the perfect fluid stress-energy tensor, the 5D, FRW field equations are of the form

$$\rho = 3\frac{\dot{R}^2}{R^2} + 3\frac{k}{R^2} + 3\frac{\dot{R}\dot{A}}{RA}$$
$$p = -[2\frac{\ddot{R}}{R} + \frac{\dot{R}^2}{R^2} + \frac{k}{R^2} + \frac{\ddot{A}}{A} + 2\frac{\dot{R}\dot{A}}{RA}]$$
$$p_5 = -3\left(\frac{\ddot{R}}{R} + \frac{k}{R^2} + \frac{\dot{R}^2}{R^2}\right) \quad (2)$$

where a dot denotes a time derivative, and p, ρ *and* p_5 represent the energy density, pressure in 4D and 1D extra dimension spaces respectively.

We consider a flat space-time (k=0) with an expansion speed in extra dimension is constant (A=0), then, take into account the fact that the universe fluid is perfect ($p = w\rho$) we will get the following equation:

$$\dot{H} + \frac{3}{2}(1+w)H^2 + \left(\frac{2+3w}{2}\right)\left(\frac{c}{ct+c_0}\right)H\frac{\dot{A}}{A} = 0 \quad (3)$$

where c, c_0 are integration constants and H is the Hubble parameter. The form of the equation is

$$\hat{H}(t) = \frac{(2+3w)}{-3(\hat{t}-1)(1+w)+(2+3w)} \quad (4)$$

Where

$$H_0 t_0 = \tau = 1, \frac{t}{t_0} = \hat{t}, \hat{H} = \frac{H}{H_0}$$

Now we obtain the following fig1

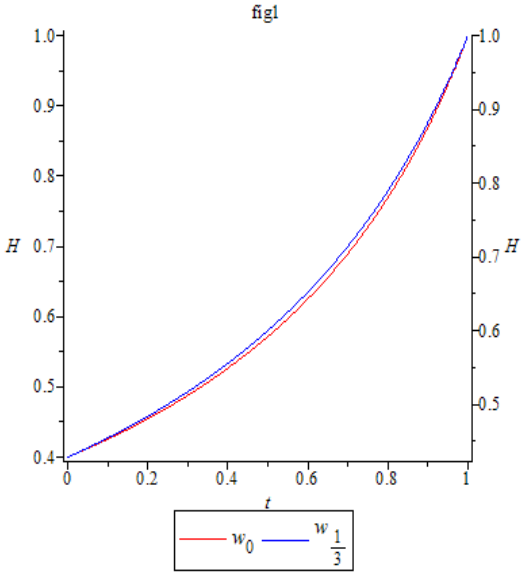

$$\frac{dH}{dt} = H^2(1-q) \Rightarrow q = \frac{\frac{dH}{dt}+H^2}{-H^2},$$

notice that $H > 0$ (see fig1), then q<0. We deduce that the universe is in accelerated expansion.

III. DYNAMICAL STUDY I

We will write the Friedmann equations as a function of Hubble parameter H_R, ρ and $H_A$according the first Friedmann equation we find:

$$\dot{H}_A = \left(\frac{2\gamma+1}{3} - w\right)\rho - {H^2}_A - 3H_R H_A$$

$$\dot{H}_R = -(1+\gamma)\frac{\rho}{3} - {H^2}_R + H_R H_A \quad (5)$$
$$\dot{\rho} = -[3H_R(1+w) + H_A(1+\gamma)]\rho$$

the analysis leads to the following cases:

if $w, \gamma > 0$, we find the critical point$\rho = 0,\ H_R = 0, H_A = 0$, which correspond to a flat and static space for 4D universe and for 1D extra dimensional space.

If $\gamma = -1\ and\ w = -1$, one has the following critical points: $\cdot\ \rho = 0, H_R = 0, H_A = 0$, which correspond to a flat and static space for $4D$ universe and for $1D$ extra dimensional space.

$\cdot\ H_R = 0, H_A = 1.101$, such that , it corresponds to a static space for $4D$ universe and an accelerated $1D$ extra dimensional space. Figure(2) displays the phase portrait for critical point $\{(H_R, H_A) = (0,1.101)\}$,such that we have a "saddle node point".

$\cdot H_R = 0.545, H_A = 0.545$, such that $\rho = 6{H_A}^2 = 1.787$, it corresponds to flat space and accelerated for $4D$ universe and $1D$ extra dimensional space, figure(3) displays the phase portrait for critical point $\{(H_R, H_A) = (0.545,0.545)\}$ which is "stable nodal sink".

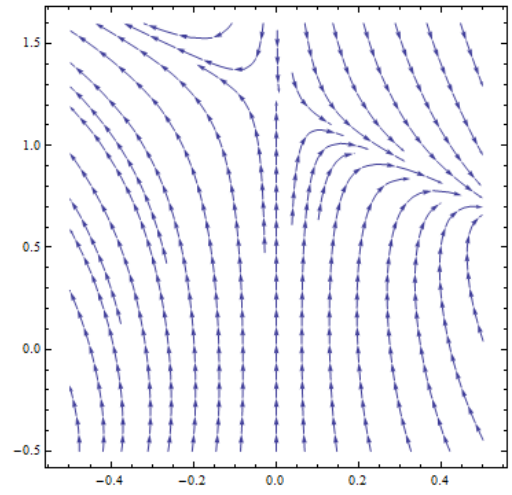

figure (2)

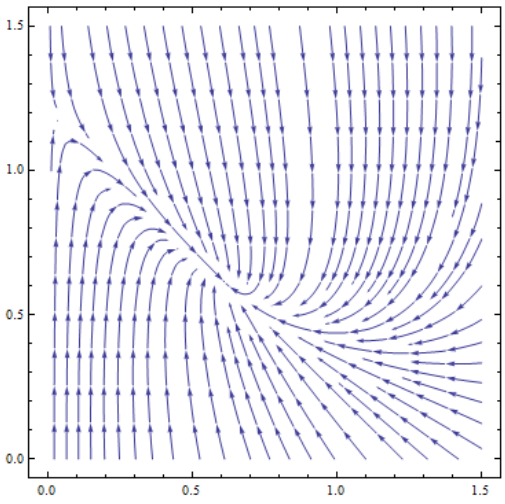

figure (3)

IV. FRIEDMAN EQUATION WITH SHEAR VISCOSITY

we consider $p = p + h(t)H_R$, equations of Friedman become

$$\rho = 3\frac{\dot{R}^2}{R^2} + 3\frac{k}{R^2} + 3\frac{\dot{R}\dot{A}}{RA}$$

$$\rho = 3\frac{\dot{R}^2}{R^2} + 3\frac{k}{R^2} + 3\frac{\dot{R}\dot{A}}{RA}$$

$$p = -\left[2\frac{\ddot{R}}{R} + \frac{\dot{R}^2}{R^2} + \frac{k}{R^2} + \frac{\ddot{A}}{A} + 2\frac{\dot{R}\dot{A}}{RA}\right] - \mathrm{h(t)}H_R \qquad (6)$$

$$p_5 = -3\left(\frac{\ddot{R}}{R} + \frac{k}{R^2} + \frac{\dot{R}^2}{R^2}\right)$$

We consider $h(t) = \alpha H$, and by using the equation p=wρ we find the expression:

$$\hat{H}(t) = \frac{(2+3w)}{-9(\hat{t}-1)(1+w)+2(2+3w)} \qquad (7)$$

Then, we obtain the following figure:

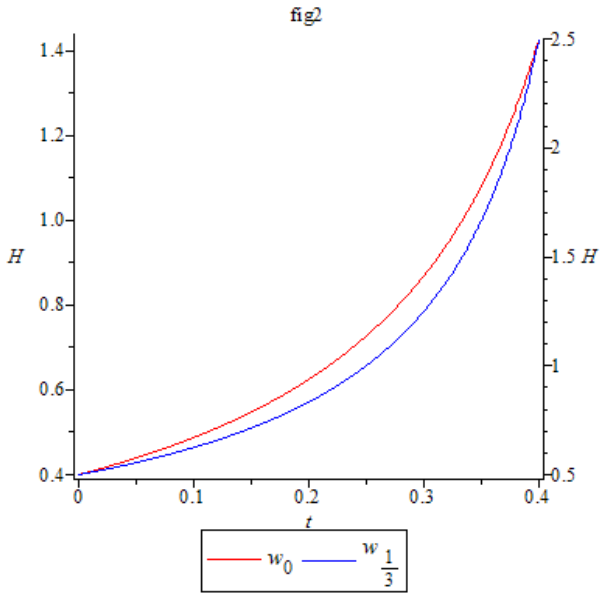

$\hat{H} > 0\ and\ \frac{d\hat{H}}{dt} > 0\ \rightarrow q < 0$, there is an accelerated expansion

V. DYNAMICAL STUDY II

In the same way we find these dynamical equations

$$\dot{H}_A = \left(\frac{2\gamma+1}{3} - w\right)\rho - {H^2}_A - 3H_R H_A - \alpha H_R$$

$$\dot{H}_R = -(1+\gamma)\frac{\rho}{3} - {H^2}_R + H_R H_A \qquad (8)$$

$$\dot{\rho} = -[3H_R(1+w) + H_A(1+\gamma)]\rho - 3\alpha {H^2}_R$$

taking in account finally, we obtain these critical points

1) $H_R = -0.5\gamma^2\frac{\alpha}{2+\gamma^2-3\gamma w}$, $H_A = 0.5\frac{\alpha\gamma(2+\gamma)}{2+\gamma^2-3\gamma w}$

$\rho = -\left(\frac{1.5\alpha^2\gamma^3}{(2+\gamma^2-3\gamma w)^2}\right)$

2) $H_R = 0$, $H_A = 0$, $\rho = 0$

VI. DISCUSSION

The critical points are defined such that:

$$2 + \gamma^2 - 3\gamma w \neq 0$$

the region $(w < 0)$ give us value negative of pressure (dark energy).

For an accelerated expansion in 4 dimensions it must

For the first point $\rightarrow \begin{cases} \alpha < 0 \\ 2 + \gamma^2 - 3\gamma w > 0 \end{cases}$

for positive values of the energy density we must have $\gamma < 0$. Figure 3 displays the allowed values of w and γ.

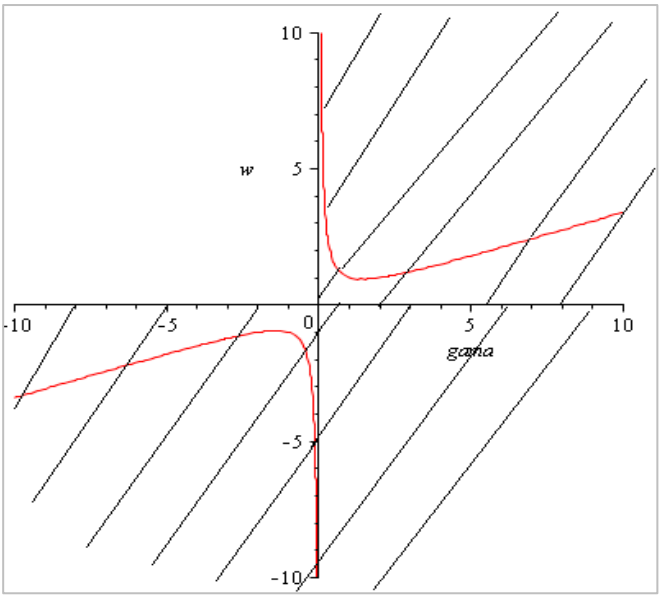

Example :

For $\gamma = -1, w = 1, \alpha = -1$, and in order that the eigenvalues are defined, we must have $(w > -1)$. This leads to a phase portrait of a (Nodal Sink) type.

For the second point

$$\gamma > 0 \rightarrow \begin{cases} \alpha > 0 \\ 2 + \gamma^2 - 3\gamma w < 0 \end{cases}$$

Or

$$\begin{cases} \alpha < 0 \\ 2 + \gamma^2 - 3\gamma w > 0 \end{cases}$$

This is impossible because it give us $\rho < 0$

VII. CONCLUSION

In this work we have studied a model of 1D extra dimension, and have considered that our universe has a viscous . We tried to find exact solutions, and make a dynamical study for the general case. The obtained results indicate that the FRW model with viscous fluid is viable and give an accelerated expansion without dark energy.

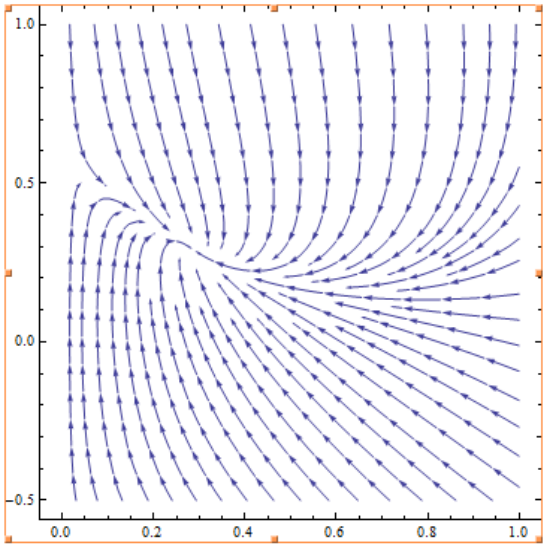

figure 7

ACKNOWLEDGMENT

We are very grateful to the Algerian Ministry of education and research as well as the DGRSDT for the financial support.

REFERENCES

[1] A.G. Riess et al. (1998) Astron. J.1161009.
[2] S. Perlmutter et al. (1999) Astrophys. J.517565.
[3] A.G. Riess et al. (2004) Astrophys. J.607665.
[4] P. Astier et al. (2006) Astron. and Astrophys.44731.
[5] D.N. Spergel et al. (2006) arXiv : astro-ph/0603449.
[6] W.H. Wood-Vasey et al. (2007) arXiv: astro-ph/0701041.
[7] T.M. Davis et al. (2007) arXiv: astro-ph/0701510.
[8] C.L. Bennett et al. (2003)Astrophys. J. Suppl.1481.
[9] D.N. Spergel et al. [WMAP Collaboration] (2003) Astrophys. J. Suppl.148175
[10] N. Mohammedi, Phys.Rev. D 65, 104018 (2002) (hep-th/0202119).
[11] Chad A. Middleton and Ethan Stanley (2011) arXiv: 1107.1828v2.